



# Optical investigation of microcircuit computations in mouse primary visual cortex

## Citation

Jaffe, Anna. 2022. Optical investigation of microcircuit computations in mouse primary visual cortex. Doctoral dissertation, Harvard University Graduate School of Arts and Sciences.

## Permanent link

<https://nrs.harvard.edu/URN-3:HUL.INSTREPOS:37371150>

## Terms of Use

This article was downloaded from Harvard University's DASH repository, and is made available under the terms and conditions applicable to Other Posted Material, as set forth at <http://nrs.harvard.edu/urn-3:HUL.InstRepos:dash.current.terms-of-use#LAA>

## Share Your Story

The Harvard community has made this article openly available.  
Please share how this access benefits you. [Submit a story](#).

[Accessibility](#)

HARVARD UNIVERSITY  
Graduate School of Arts and Sciences



DISSERTATION ACCEPTANCE CERTIFICATE

The undersigned, appointed by the  
Division of Medical Sciences  
Program in Neuroscience  
have examined a dissertation entitled

*Optical investigation of microcircuit computations in mouse primary  
visual cortex*

presented by Anna Wang Jaffe  
candidate for the degree of Doctor of Philosophy and hereby  
certify that it is worthy of acceptance.

Signature: 


Typed Name: Dr. Rachel Wilson

Signature: 

Typed Name: Dr. John Assad

Signature: 

Typed Name: Dr. Richard Born

Signature: 

Typed Name: Dr. Jerry Chen

Date: January 11, 2022



Optical Investigation of Microcircuit Computations in Mouse Primary Visual Cortex

a dissertation presented

by

Anna Wang Jaffe

to

The Division of Medical Sciences

in partial fulfillment of the requirements

for the degree of

Doctor of Philosophy

in the subject of

Neurobiology

Harvard University

Cambridge, Massachusetts

January 2022

©2022 – Anna Wang Jaffe  
All rights reserved.

## Optical Investigation of Microcircuit Computations in Mouse Primary Visual Cortex

## ABSTRACT

A fundamental challenge of visual cortical neuroscience is to understand how sensory representations are transformed within and across layers of primary visual cortex ( $V_1$ ). Visual signals are thought to propagate in a feedforward manner from the retina to the thalamus and then through the layered structure of  $V_1$ , from layer 4 ( $L_4$ ) to layer 2/3 to layer 5. Here, we address one major step of visual processing: how are representations transformed within  $L_4$ , the primary input layer of  $V_1$ ? We first developed a strategy to label neurons in  $L_4$ . To understand computations during visual processing in awake animals, we then employed influence mapping, an approach developed by our lab to causally manipulate neural activity using *in vivo* single-neuron optical perturbations. We performed simultaneous two-photon optogenetic photostimulation of targeted individual neurons while imaging the responses of neighboring populations. By relating the influence of a neuron on other cells to their visual tuning properties, the computational function of neural activity patterns can then be inferred. Using this technique, we found that excitatory neurons in  $L_4$  strongly recruited activity from nearby but not distant cells, which was dependent on similarity in activity and certain tuning features such as preferred orientation and receptive field overlap. This result supports the idea that  $L_4$  amplifies visual signals via a feature-specific like-excites-like motif. These experiments have advanced our understanding of local transformations within  $L_4$  of  $V_1$ . In addition, the technical approaches developed serve as a foundation for future studies of laminar cortical mechanisms that underlie visual processing, including comparing the transformations that occur within and between layers.

# Contents

TITLE	i
COPYRIGHT	ii
ABSTRACT	iii
CONTENTS	iv
LIST OF FIGURES	vii
LIST OF TABLES	viii
ACKNOWLEDGMENTS	ix
<b>I INTRODUCTION</b>	<b>I</b>
1.1 Laminar substructure of cortex . . . . .	2
1.2 Tuning properties within V <sub>I</sub> . . . . .	3
1.3 Organization of thalamocortical and cortico-cortical connectivity . . . . .	3
1.4 Relationship of connectivity to tuning properties . . . . .	5
1.5 Theories of cortical computation in L <sub>4</sub> . . . . .	6
1.6 New technologies for probing microcircuit computations . . . . .	8
1.6.1 Background . . . . .	8
1.6.2 Previous work on two-photon single-neuron stimulation . . . . .	10
1.6.3 Characterizing neuron-neuron influence to understand computations . . . . .	11
1.7 Roadmap . . . . .	12
<b>2 SINGLE-NEURON PHOTOSTIMULATION IN L<sub>4</sub></b>	<b>13</b>
2.1 Contributions . . . . .	13
2.2 Introduction . . . . .	14
2.3 Distinctive population activity in CaMKII-tTA;tetO-GCaMP6s mice . . . . .	14
2.3.1 Comparing neural activity across mouse lines . . . . .	14
2.3.2 Doxycycline treatment . . . . .	17
2.4 Setup for single-neuron photostimulation experiments . . . . .	18

2.5	Methods . . . . .	22
2.5.1	Animals and surgery . . . . .	22
2.5.2	Visual stimuli for experiments comparing neural activity across mouse lines . . . . .	24
2.5.3	Widefield retinotopic imaging . . . . .	24
2.5.4	Microscope design . . . . .	25
2.5.5	Photostimulation protocol . . . . .	26
2.5.6	Imaging data pre-processing . . . . .	28
<b>3</b>	<b>INFLUENCE MAPPING SHOWS SIGNATURES OF AMPLIFICATION IN V<sub>I</sub> L<sub>4</sub></b>	<b>30</b>
3.1	Introduction . . . . .	30
3.2	Experimental design . . . . .	31
3.2.1	Magnitude of neural responses during experimental blocks . . . . .	32
3.3	Calculation of influence . . . . .	32
3.4	Tuning within L <sub>4</sub> . . . . .	37
3.4.1	Random gratings tuning and Gaussian process regression . . . . .	37
3.4.2	Gaussian noise movies and receptive field measurement . . . . .	41
3.5	Influence regression . . . . .	46
3.6	Methods . . . . .	54
3.6.1	Visual stimuli . . . . .	54
3.6.2	Experimental protocol . . . . .	55
3.6.3	Seeding block-specific processing . . . . .	57
3.6.4	Photostimulation-specific pre-processing . . . . .	57
3.6.5	Neuron response magnitude to photostimulation and random gratings . . . . .	58
3.6.6	Influence calculations . . . . .	58
3.6.7	Gaussian process regression and tuning . . . . .	59
3.6.8	Gaussian noise movies . . . . .	63
3.6.9	Receptive field measurement . . . . .	63
3.6.10	Influence regression and associated analyses . . . . .	66
3.6.11	Statistics . . . . .	67
<b>4</b>	<b>DISCUSSION AND FUTURE EXPERIMENTS</b>	<b>68</b>
4.1	Feature-specific amplification within V <sub>I</sub> L <sub>4</sub> . . . . .	68
4.1.1	Summary . . . . .	68
4.1.2	Comparison to previous results . . . . .	70
4.1.3	Function of amplification . . . . .	70
4.2	Utility of influence mapping . . . . .	71
4.3	Modifications and additional experimental directions . . . . .	72
4.3.1	Influence at the population versus single-neuron level . . . . .	72



4.3.2	Decreasing opsin density to improve photostimulation resolution . .	73
4.3.3	Alternative visual stimuli . . . . .	73
4.3.4	Inhibition in L4 . . . . .	74
4.3.5	Transformations between cortical layers . . . . .	75
4.3.6	Other extensions . . . . .	77
4.4	Conclusion . . . . .	77

REFERENCES		87
------------	--	----

# List of figures

2.1	Comparison of visual responses and activity correlations in L <sub>2/3</sub> between mouse lines. . . . .	16
2.2	Labeling strategy for L <sub>4</sub> single-neuron photostimulation experiments. . . . .	19
2.3	Photostimulation responses of targeted sites . . . . .	21
2.4	Optical layout of the custom-built ETL- and SLM-based two-photon <i>in vivo</i> photostimulation microscope. . . . .	27
2.5	Sources and labels from CNN for an example L <sub>4</sub> session . . . . .	29
3.1	Schematic of experimental protocol . . . . .	33
3.2	The magnitude of V <sub>I</sub> L <sub>4</sub> targeted neuron responses to photostimulation and visual stimuli. . . . .	34
3.3	Influence characterization in L <sub>4</sub> . . . . .	38
3.3	(continued) . . . . .	39
3.4	Example tuning and activity characterization of L <sub>4</sub> neurons using Gaussian processes. . . . .	42
3.5	Characterization of V <sub>I</sub> L <sub>4</sub> tuning using GP regression. . . . .	43
3.6	Gaussian noise movies and linear RF characterization. . . . .	47
3.6	(continued) . . . . .	48
3.7	Relationship between cortical distance, activity metrics, tuning components, RF components, and influence. . . . .	50
3.7	(continued) . . . . .	51

# List of tables

2.1	Doxycycline treatments for CaMKII-tTA;tetO-GCaMP6s mice. . . . .	17
3.1	Significantly tuned neurons for each tuning dimension, from GP regression. .	63

# Acknowledgments

I am extremely grateful to have had the opportunity to work with my advisor, Chris Harvey, who has provided excellent training in scientific thinking and writing and supported me through my interests, and also cultivated an environment of scientific freedom and rigor. I feel truly lucky to have gotten to learn from Chris during my time in his lab.

To members of the lab, past and present, who have been incredible colleagues and friends: I could not have asked for better people to do science with throughout the course of my PhD. I have learned so much from everyone and the conversations we have had. Special thanks to Matthias Minderer, Selmaan Chettih, Noah Pettit, Jim Robinson-Bohnslav, and Shih-Yi Tseng, of course for science, but also for general shenanigans and being G-olds (in spirit, at the very least) together; Sofia Soares and Charlotte Arlt, for friendship and being inspirational women to look up to; and Dan Wilson, for camaraderie and project and moral support in equal bounds.

I would like to thank the friends I have made in PiN, and especially my classmates, who have made this experience more enjoyable than I could have imagined. Thank you to Mélanie, Mehak, Hannah, and Genelle, who have been an amazing group of women to navigate graduate school with; and Kelsey and Rachel, for holding it down on Fuller Street over the past few years, including during a global pandemic. Thanks also to friends from undergrad and earlier for keeping me anchored to life and fun outside the PhD bubble.

Thank you to my preliminary qualifying exam-turned dissertation advisory committee: Mark Andermann, Bernardo Sabatini, and Rachel Wilson, for useful feedback and guidance throughout the course of my graduate career. I thank my exam committee, John Assad, Rick Born, and Jerry Chen, for taking the time to provide feedback on my dissertation. I also thank my SAC advisor, Chinfei Chen, for scientific and personal advice, as well as Karen Harmin and Susan Jackson for keeping the Program in Neuroscience running so smoothly.

Finally, most importantly, I would like to thank my brother and parents – Jack, Zhenhua, and Bruce – as well as my extended family, for their unconditional support.

# 1

## Introduction

Understanding the neural mechanisms underlying visual processing requires probing the computations and function of microcircuits in cortical layers. How visual representations differ between layers and how neurons reshape these representations locally or by transforming incoming information is a primary question of cortical physiology. Here, we aim to understand detailed laminar cortical transformations in the context of visual perception. By using new technologies for targeted spatiotemporal neural perturbations while monitoring population responses, we can derive mechanistic circuit-based theories of laminar sensory transformations. By causally char-

acterizing the principles of circuit computations in V<sub>I</sub>, and L<sub>4</sub> in particular, we aim to provide insight into the fundamental mechanisms that support vision.

## 1.1 LAMINAR SUBSTRUCTURE OF CORTEX

V<sub>I</sub> is known to process sensory information through a layered architecture. Decades of anatomical and physiological studies have led to the classic model of information flow in cortex: thalamus sends ascending projections to L<sub>4</sub>, which strongly innervates layer 2/3 (L<sub>2/3</sub>), and then L<sub>2/3</sub> passes input to layer 5 (Douglas and Martin, 2004; Felleman and Van Essen, 1991; Gilbert, 1983; Harris and Shepherd, 2015; Lefort et al., 2009; Miller, 2016; Thomson, 2007). Support for feed-forward processing also comes in part from work showing that L<sub>4</sub> receives little feedback excitatory input (Coogan and Burkhalter, 1993; Harris et al., 2019; Lefort et al., 2009); this anatomical pathway is also consistent with function, as optogenetic stimulation of L<sub>2/3</sub> pyramidal neurons does not generate activity in L<sub>4</sub> (Adesnik and Scanziani, 2010).

Substantial evidence from studies across species highlights the cellular specialization within cortical layers, as cell densities vary across layers, distinct molecular markers can robustly label individual layers, and different cell types can be further classified by their morphology, electrophysiology, and transcriptomic profiles (Douglas and Martin, 2004; Harris and Shepherd, 2015; Keller et al., 2018; Tasic et al., 2016, 2018). For example, L<sub>4</sub> of mouse V<sub>I</sub> can be genetically labeled with Cre lines for *Nr5a1*, *Rorb*, and *Scnn1a* (Harris et al., 2019; Madisen et al., 2010), and contains mostly spiny neurons with a pronounced apical dendrite (e.g., star pyramids or pyramidal neurons), some of which have tufts in L<sub>1</sub> (Gouwens et al., 2019; Scala et al., 2019).

## 1.2 TUNING PROPERTIES WITHIN V<sub>I</sub>

V<sub>I</sub> neurons fire in response to visual stimuli and show tuning to different visual features. Layers in V<sub>I</sub> show some degree of functional specialization, as silicon probe recordings and two-photon calcium imaging have provided evidence that visual receptive field structure and response properties can vary across layers. For example, in cat V<sub>I</sub>, deeper thalamorecipient layers contain mostly simple cells, whereas cells in more superficial layers tend to be complex and have heterogeneous receptive field structures that are stereotyped by laminar position (Gilbert, 1977; Hubel and Wiesel, 1962; Martinez and Alonso, 2001; Martinez et al., 2005). In tree shrew V<sub>I</sub>, orientation tuning in L<sub>4</sub> is largely absent but is present in superficial layers (Chisum et al., 2003; Mooser et al., 2004). In mouse V<sub>I</sub>, L<sub>4</sub> shows higher direction selectivity compared to L<sub>2/3</sub> and L<sub>5</sub> (Niell and Stryker, 2008; Sun et al., 2016; de Vries et al., 2020). Additional evidence for the idea that response properties vary as a function of layer has been shown across sensory modalities in studies of rodent visual, somatosensory, and auditory cortices (Barbour and Callaway, 2008; Brecht et al., 2003; Shepherd, 2005; de Vries et al., 2020). Cortical layers may therefore receive feedforward input and also locally transform incoming signals, such that each stage of processing may have a unique functional role.

## 1.3 ORGANIZATION OF THALAMOCORTICAL AND CORTICO-CORTICAL CONNECTIVITY

Significant effort has gone toward characterizing the principles of sensory cortical connectivity. Neurons in cortex are highly interconnected and show recurrent activity, with the largest synaptic input coming from neighboring cells (Benshalom and White, 1986; Binzegger, 2004; Douglas



and Martin, 2004; Rodney et al., 1995; Seeman et al., 2018; Thomson, 2007). Visual information is relayed to V1 via thalamic dorsolateral geniculate nucleus (dLGN) inputs to L4, with thalamocortical projections to L4 in cat striate cortex constituting <10% of synapses (da Costa and Martin, 2009) and 15-30% in L4 of mouse V1, primary somatosensory cortex (S1), and primary motor cortex (Arkhipov et al., 2018; Bopp et al., 2017). This suggests that the majority of excitatory inputs come from other local cortico-cortical connections, although L4 neurons are also strongly driven by thalamic inputs (Harris and Mrsic-Flogel, 2013; Petersen, 2007). In general, connections between V1 L4 neurons appear to be sparser but stronger than between neurons within L2/3 (Cossell et al., 2015; Ko et al., 2011; Seeman et al., 2018)

Of interest is whether connections and their strengths are random throughout cortical populations. *In vitro* slice work has addressed pairwise monosynaptic connectivity between cell types and cortical layers and demonstrated that neurons show nonrandom connections. Through simultaneous whole-cell recordings in rat V1 L5, reciprocal network motifs and mutually connected triplets have been found to be present at above-random chance within small distances; further, synaptic strengths are skewed and follow a lognormal distribution, such that most excitatory postsynaptic potentials are small and weights are strongest among a limited number of connections (Song et al., 2005). This non-uniform connectivity has also been found in other layers and in barrel cortex (Feldmeyer et al., 2002; Lefort et al., 2009; Markram et al., 1997). Mutual interconnection motifs in larger sets of neurons distributed over greater areas are also over-represented and are best described by a clustering rule, where neurons that share more common neighbors also have a higher connection probability (Perin et al., 2011). Other studies have also provided evidence for higher-order patterns within cortical networks. Connected pairs in mouse V1 L4 share more dLGN inputs than unconnected pairs, and connected pairs of L4 and L2/3

neurons are contacted by the same thalamocortical axons (Morgenstern et al., 2016). In addition, subnetworks of fast-spiking interneurons in rat V1 preferentially connect to L2/3 pyramidal neurons that provide them with excitatory input, and both connected L2/3 pyramidal cells and reciprocally connected excitatory-inhibitory pairs share common excitatory input from L4 and within L2/3 (Yoshimura and Callaway, 2005; Yoshimura et al., 2005).

#### 1.4 RELATIONSHIP OF CONNECTIVITY TO TUNING PROPERTIES

Connectivity is also related to function, as excitatory neurons that are synaptically connected tend to have similar visual response properties. Studies combining *in vivo* two-photon calcium imaging with *in vitro* whole-cell recording in L2/3 of mouse V1 have shown that excitatory neurons follow a “like-to-like” connectivity principle: nearby (i.e.,  $<250\ \mu\text{m}$  apart) neurons with similar orientation tuning have a higher probability of connecting (Ko et al., 2011), and the few strong connections that exist are between cells with similar spatial receptive fields and response correlation (Cossell et al., 2015). Of note is that this connectivity architecture in mice does not require spatial clustering of neurons with shared orientation selectivity as in V1 of other species such as primates or cats (Ohki et al., 2005). A study using functional imaging and large-scale electron microscopy (EM) reconstruction in an excitatory network in mouse V1 L2/3 provided confirmation of previous imaging and electrophysiology work, showing that pyramidal neurons preferentially synapse onto other neurons with similar orientation selectivity, and these synapses are also larger (Lee et al., 2016). Another set of studies in mouse V1 used transsynaptic retrograde tracing with two-photon imaging and found that presynaptic networks of single L2/3 pyramidal neurons form layer-specific modules, as cells within each layer exhibit similar motion direction tuning, and these are also sometimes locked to the preference of the starter postsynaptic cell

(Wertz et al., 2015); furthermore, presynaptic excitatory neurons in L4 and L2/3 are distributed coaxially in cortical space to the postsynaptic neuron's preferred orientation (Rossi et al., 2020). Together, these data suggest that fine-scale cortical subnetworks that are co-tuned for particular visual features mediate processing of sensory information.

## 1.5 THEORIES OF CORTICAL COMPUTATION IN L4

A next step after characterizing connectivity and neural functional properties is to understand how connections give rise to computations, or processes by which representations of information are transformed into a new form, and what those computations are. Within recurrent cortical circuits, relating the functional properties of a neuron (e.g., visual tuning) to its relationship on the activity of other cells in the population can then be used to infer the computational function of a microcircuit. Layer-specific manipulations can be used to test hypotheses about what cortical layers may compute during processing of sensory information.

Computations within L4 and L2/3 of V1 have been well-studied in other species, and L2/3 has been heavily studied within the context of mouse V1, but there is comparatively less known about mouse V1 L4. A number of studies in mice have shown that LGN contains neurons that are already orientation selective (Li et al., 2013b; Lien and Scanziani, 2013; Marshel et al., 2012; Piscopo et al., 2013; Scholl et al., 2013; Zhao et al., 2013), and recent work has used two-photon *in vivo* calcium imaging of LGN axons in V1 L4 to determine whether thalamic inputs in cortex are selective. One study found that  $\sim 18\%$  of LGN inputs were orientation selective (Kondo and Ohki, 2016), and another found that  $\sim 50\%$  of boutons in thalamorecipient L4 are orientation- and direction-tuned; moreover, the preferred tuning of L4 neurons is strongly biased towards those of the thalamic inputs (Sun et al., 2016), suggesting that tuned thalamic inputs directly

contribute to tuning in cortex. However, selectivity is not identical between LGN boutons and L4 neurons, as cortical neurons show sharper tuning and greater diversity of preferred orientation and direction than thalamocortical boutons, pointing towards the hypothesis that recurrent computations within L4 further transform incoming sensory information. A related proposed model of information processing in L4 is that intracortical connections amplify thalamic inputs. Two studies of mouse V1 L4 (Li et al., 2013b; Lien and Scanziani, 2013) have assessed the role of thalamic and excitatory intracortical circuits by isolating thalamocortical projections. Cortical excitatory recurrence was silenced by activating channelrhodopsin-expressing parvalbumin inhibitory neurons, which densely innervate pyramidal cells. Thalamic and cortical tuning for orientation and temporal phase are the same, and thalamic excitation to a L4 neuron contributes ~30% of the total excitation (i.e., recurrent cortical connectivity provides the remaining 70% of excitation within L4). Intracortical excitation linearly amplifies current amplitude from thalamic inputs without changing orientation or direction tuning properties, and L4 receptive field size increases without changing shape. Together, these results suggest that L4 amplifies inputs from thalamus, although the mechanism by which this occurs has not been fully elucidated experimentally.

Computational models constrained by experimental measurements have proposed that L4 selectivity arises from convergent LGN inputs and recurrent excitatory like-to-like connectivity that amplifies thalamic signals; excitation is also then counteracted by local inhibition (Arkhipov et al., 2018; Billeh et al., 2020; Rodney et al., 1995; Somers et al., 1995; Van Vreeswijk and Sompolinsky, 1996). One of these studies constructed a model of mouse V1 L4 using a network of biophysically-realistic models of individual neurons (Arkhipov et al., 2018), finding that many properties of the final model were consistent with previously demonstrated experimental results

(Li et al., 2012; Reinhold et al., 2015; Yoshimura et al., 2005), including that the levels of orientation selectivity in L4 are similar to those measured physiologically. Together, the aforementioned experimental and theoretical results suggest that regardless of the exact information content of thalamocortical signals, intracortical circuits in L4 amplify components of feedforward thalamic inputs. This proposed mechanism for amplification is also supported by *in vitro* experiments showing that connected pairs of L4 neurons share more thalamic inputs than unconnected pairs (Morgenstern et al., 2016). Cortical subnetworks are generally tuned for similar sensory features, so recurrent excitation can increase the number of neurons that respond to a given stimulus, prolonging sensory responses. This mechanism increases efficacy and allows for more efficiently driving downstream targets, which has the added benefit of making the system more robust to noise. However, an open question is whether L4 actually contains like-excites-like motifs, in which neurons preferentially excite other neurons with similar responses to specific visual features. Although an amplification model has been proposed by previous work, it has not been directly tested experimentally because it requires a functional and causal measure of one neuron's influence on another.

## 1.6 NEW TECHNOLOGIES FOR PROBING MICROCIRCUIT COMPUTATIONS

### 1.6.1 BACKGROUND

Theoretical studies and anatomy or connectivity-based experiments using techniques such as tracing, electrophysiology, EM, or *in vivo* recordings to understand V1 circuits have generated hypotheses for potential cortical transformations, but mapping microcircuits at the level of synapses or single cells has been a significant technological challenge. Characterizing recurrent connectivity is difficult because the majority of synaptic connections are weak and sparse (Lefort et al.,

2009; Scala et al., 2019; Seeman et al., 2018; Song et al., 2005). Using paired recording experiments to predict functional responses and how activity in a neuron affects local networks is difficult and low-throughput due to limitations in the number of neurons (up to  $\sim 10$ ) that can be patched simultaneously (Cossell et al., 2015; Guzman et al., 2016; Peng et al., 2019). In addition, long-range connections in brain slices are often not maintained. It is unclear whether principles for the logic of cortical computations as determined from analyzing small numbers of neurons generalize to larger networks. Furthermore, contributions from sources such as polysynaptic pathways, nonlinear processing in dendrites, or intrinsic neuronal properties are also unknown. Studies of V1 circuits have also often used perturbations with coarse spatial and temporal resolution or lacked causal manipulations entirely. In addition, observations of neural activity are unable to provide causal explanations for the mechanisms that underlie sensory processing. Nevertheless, the extensive literature on the physiology of cortical circuits, as well as more recent optogenetics and imaging studies, have produced a multitude of testable hypotheses.

To obtain a full understanding of cortical computations, the ideal requisite tools include noninvasively recording from many neurons across layers and identifying their cell type, perturbations that allow targeting of specific neurons with fine spatiotemporal precision, and obtaining behavioral data such as running patterns or arousal/attention. In addition to sophisticated genetic tools for rodents that enable the dissection of cell type-specific circuits, newer experimental methods for two-photon cellular-resolution optical manipulation and readout of neural activity are now available. Advantages include the ability to target individual neurons with specific functional properties and using more physiological stimulation patterns, unlike in one-photon optogenetic experiments in which an entire genetically-defined cell population is illuminated simultaneously. These technologies have opened promising new avenues for interrogating microcircuit compu-

tations.

### 1.6.2 PREVIOUS WORK ON TWO-PHOTON SINGLE-NEURON STIMULATION

Numerous approaches for simultaneous two-photon optogenetics and calcium imaging have recently been developed and applied to study neural circuits (Bègue et al., 2013; Chettih and Harvey, 2019; Daie et al., 2021; Dalgleish et al., 2020; Gill et al., 2020; Marshel et al., 2019; Packer et al., 2012, 2015; Pégard et al., 2017; Rickgauer and Tank, 2009; Robinson et al., 2020). Broadly, these can be divided by differences in genetically-encoded calcium indicators, optogenetic actuators, and stimulation and imaging methods. To use opsins in combination with GCaMP, many studies have used red-shifted opsins. Methods for photostimulation can be split by scanning or parallel illumination. Scanning involves sweeping a diffraction-limited spot across the soma (Packer et al., 2012; Prakash et al., 2012; Rickgauer and Tank, 2009), whereas parallel illumination (e.g., with computer-generated holography or generalized phase contrast and temporal focusing) sculpts light into multiple spots or extended patterns, including in 3D (Andrasfalvy et al., 2010; Bègue et al., 2013; Chaigneau et al., 2016; dal Maschio et al., 2017; Hernandez et al., 2016; Mardinly et al., 2018; Papagiakoumou et al., 2010; Pégard et al., 2017; Shemesh et al., 2017). Studies have also combined spatial light modulator-based light patterning with galvanometer (galvo) scanning, where excitation spots are focused on multiple cells and galvos are used to scan the beamlets over an area corresponding to cell bodies (Packer et al., 2015; Yang et al., 2018). Imaging in single planes or volumes can be achieved with a number of approaches, including sequential and parallelized scanning (dal Maschio et al., 2017; Duemani Reddy et al., 2008; Grewe et al., 2010; Katona et al., 2012; Lu et al., 2017; Prevedel et al., 2016; Song et al., 2017; Vladimirov et al., 2018; Yang et al., 2018).

### 1.6.3 CHARACTERIZING NEURON-NEURON INFLUENCE TO UNDERSTAND COMPUTATIONS

Our lab has built upon optical methods for manipulating neural activity with high spatiotemporal specificity and developed a technique called influence mapping to causally probe computations in local cortical networks in awake, behaving animals (Chettih and Harvey, 2019). Influence mapping involves targeted two-photon photostimulation of single cells while monitoring the resulting spiking activity of the neighboring neural population with known tuning. This technique is well-suited for uncovering cortical transformations because it bridges multiple levels, from monosynaptic and polysynaptic to causal functional connectivity, while also dramatically increasing the total number of neurons that can be considered. Ultimately, we are not necessarily interested in the explicit biophysical connectivity of a microcircuit, but rather the nature of the computations that result from the underlying structure. In other words, what cortical transformations exist, and how are those functionally used to support sensory perception and behavior? Influence mapping provides a convenient level of abstraction for being able to address these questions.

The previous study from our lab applied influence mapping to L2/3 of mouse V1 and found that photostimulating single neurons reduced responses in the non-targeted neural population. Influence was negatively related to signal correlations between pairs of targeted and non-targeted neurons, and tuning components such as preferred orientation contributed to negative influence. Together, these results provide causal experimental evidence that one computation L2/3 performs is feature competition, where excitatory neurons with similar visual tuning properties inhibit each other in a like-suppresses-like motif, which had previously not been described in



studies that used observations of neural activity. This work demonstrated the feasibility of using the influence mapping technique to uncover cortical computations, which could be extended to other cell types, layers, and behavioral conditions.

## 1.7 ROADMAP

Using influence mapping, we investigated the relationships between  $V_1$  L4 excitatory neurons with known tuning properties. In Chapter 2, we discuss previous work on two-photon photostimulation and the development of influence mapping in our lab. We also describe our strategy for labeling neurons and the general setup and methodology for influence mapping experiments in L4. Chapter 3 describes our application of influence mapping to understanding cortical computations within L4 of  $V_1$  of awake, behaving mice. We find that using single-neuron perturbations in L4 reveals signatures of amplification, in which neurons with certain activity patterns and visual feature preferences recruit other neurons with similar properties. Chapter 4 includes discussion of extensions to the current study of L4 in  $V_1$ , as well as potential future areas of investigation using influence mapping.

# 2

## Single-Neuron Photostimulation in L4

### 2.1 CONTRIBUTIONS

This chapter includes material modified from work published in Kafashan, Jaffe, Chettih et al., 2021.

*Author contributions: A.W.J. and S.N.C. performed the experiments; M.K., R.N., I.A.-R., R.M.-B., and J.D. developed the theory; and M.K., A.W.J., S.N.C., and J.D. analyzed the data.*

## 2.2 INTRODUCTION

Here, we describe the all-optical approach we used to probe microcircuit computations within L<sub>4</sub> of V<sub>1</sub>, as it is the primary input layer from the thalamus, and other work has generated predictions about the types of computations that may be occurring within it. We built upon previous work utilizing two-photon calcium imaging and photostimulation, including work from our lab on influence mapping.

## 2.3 DISTINCTIVE POPULATION ACTIVITY IN CaMKII-tTA;tetO-GCaMP6s MICE

To perform calcium imaging and photostimulation, co-expression of both an indicator of neural activity and an opsin is required. We tested a number of different strategies for labeling L<sub>4</sub> neurons in V<sub>1</sub>, as typical GCaMP mouse lines (e.g., Thy1-GCaMP) or conventional adeno-associated viral vectors do not robustly label neurons in L<sub>4</sub>. One genetic mouse line that we initially tested was the CaMKII-tTA;tetO-GCaMP6s transgenic, which densely labels neurons across cortical layers (Wekselblatt et al., 2016). We performed a set of pilot experiments in which we imaged L<sub>2/3</sub> or L<sub>4</sub> while awake mice were presented with 10% or 20% contrast drifting grating stimuli.

### 2.3.1 COMPARING NEURAL ACTIVITY ACROSS MOUSE LINES

We compared L<sub>2/3</sub> visual tuning between the CaMKII-tTA;tetO-GCaMP6s mice, Thy1-GCaMP6s transgenic mice (which also show cortical expression), and C<sub>57</sub>BL/6J (wild-type) mice injected with viral GCaMP6s by presenting low-contrast drifting gratings. We found that the direction and orientation tuning of individual neurons looked comparable across all mouse lines (Figure

2.1a). We then examined the relationship between signal correlations, calculated as the correlation in the mean deconvolved response, and noise correlations, calculated as the mean-subtracted residual response, between pairs of neurons. For signal and noise correlations, there was typically a weakly positive mean relationship with wide scatter. However, in the CaMKII-tTA;tetO-GCaMP6s data, the same gradual linear relationship was present, but with an additional component of many neuron pairs with highly correlated signal and noise correlations, indicating that a large number of pairs of neurons had very similar activity (Figure 2.1b). When we manually examined highly correlated neuron pairs within the CaMKII-tTA;tetO-GCaMP6s datasets, we found that the pairs came from different neurons, were in different parts of the imaging field of view, and many showed reasonable visual tuning.

We further analyzed these data as part of a study to understand how sensory information in V1 scales and if it saturates within large neural populations (Kafashan et al., 2021). In this study, we examined how V1 neurons encoded information about the drift direction of a moving visual stimulus. We compartmentalized information-limiting correlations to extrapolate information growth with population size and estimated how many neurons are required to capture 95% of the total asymptotic information ( $N_{95}$ ). In the CaMKII-tTA;tetO-GCaMP6s mice,  $N_{95}$  was 1-2 orders of magnitude lower compared to Thy1-GCaMP6s mice and wild-type mice expressing viral GCaMP (data not shown). Presumably, this difference arises from redundancy that causes information content to saturate much more quickly in the CaMKII-tTA;tetO-GCaMP6s mice. We also repeated the same experiments in L4 in a separate set of CaMKII-tTA;tetO-GCaMP6s mice and saw similar results as in L2/3 described above.

We concluded that although single-neuron activity appeared to be normal, activity at the pop-

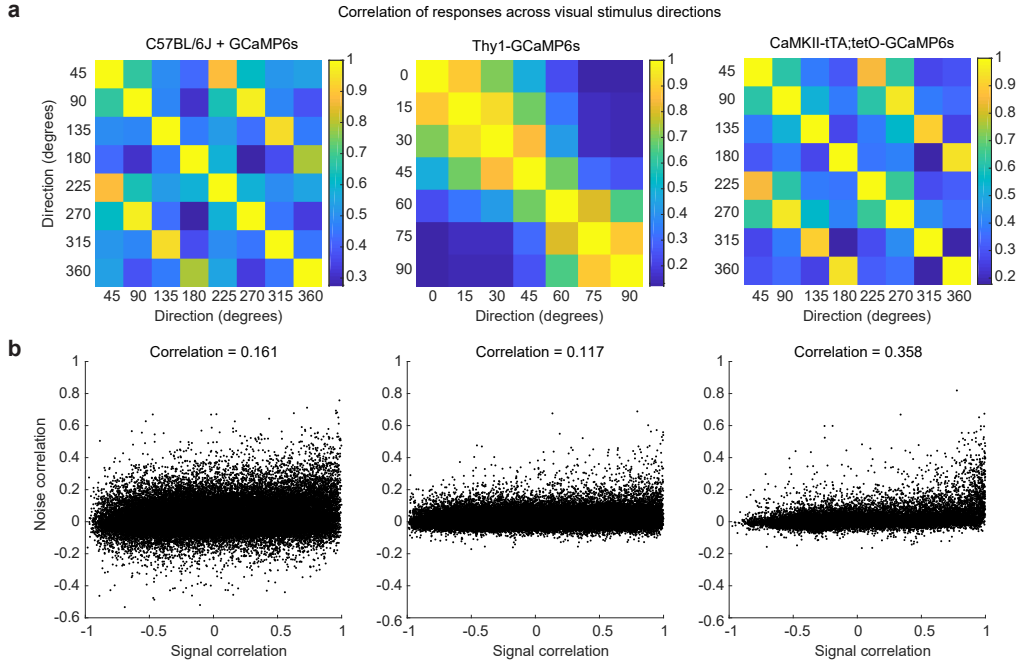


**Figure 2.1: Comparison of visual responses and activity correlations in L2/3 between mouse lines.** **a**, Example mice: left column, C57BL/6J (wild-type) mouse expressing viral GCaMP6s; middle column, Thy1-GCaMP6s transgenic mouse; right column, CaMKII-tTA;tetO-GCaMP6s transgenic mouse. Correlation of V1 L2/3 neuron responses to different directions of low-contrast drifting grating stimulus. Across all mouse lines, orientation and direction tuning is evident from higher correlations along the diagonal and off-diagonal comparisons. **b**, Correlation between signal correlation and noise correlation for pairs of neurons. Wild-type and Thy1-GCaMP6s mice show a weak positive correlation between signal and noise correlation ( $R = 0.16$ ,  $R = 0.12$ ). CaMKII-tTA;tetO-GCaMP6s shows a stronger positive relationship ( $R = 0.36$ ) due to the presence of many pairs of neurons with highly correlated signal and noise correlations.

Doxycycline (mg/ml)	Time on doxycycline (starting from birth)	GCaMP expression in L2/3
2	5+ weeks, 9+ weeks (includes before pregnancy)	Unusable; does not recover even 2+ months after doxycycline removal
0.2	1 week	Sparse, too low
	2.5 weeks	Sparse, too low
0.04	1.5 weeks	Expression is fine, but same correlation issue

**Table 2.1: Doxycycline treatments for CaMKII-tTA;tetO-GCaMP6s mice.**

ulation level was qualitatively different in the CaMKII-tTA;tetO-GCaMP6s mice compared to the other lines. Furthermore, the neuron pairs with highly-correlated signal and noise correlations in these mice appeared to be abnormal not only compared to our measurements in other mouse lines, but also to other work on correlations across species, brain areas, and behavioral tasks. These studies showed that there is a positive relationship between tuning similarity and trial-to-trial variability in activity, as we also observed in all experimental cases, but none described the presence of neuron pairs with highly-correlated signal and noise correlations as we observed in CaMKII-tTA;tetO-GCaMP6s mice (Averbeck and Lee, 2003; Bartolo et al., 2020; Kohn and Smith, 2005; Okun et al., 2015).

### 2.3.2 DOXYCYCLINE TREATMENT

We attempted to mitigate concerns of aberrant neural population activity in the CaMKII-tTA;tetO-GCaMP6s mice by raising mothers and pups from breeding pairs on doxycycline (Table 2.1) to suppress GCaMP expression until later in development. To evaluate whether doxycycline treatments were effective, we performed the same imaging experiments as described above after pups reached at least 8 weeks of age. Mice received doxycycline orally in drinking water with 5% sucrose (Steinmetz et al., 2017).

Under the highest dosage of doxycycline tested (2 mg/ml), we found that raising pregnant moth-

ers and pups on this dosage for even five weeks resulted in GCaMP levels that were too low to be usable for imaging and did not increase to reasonable levels even after months following cessation of doxycycline treatment. We then decreased doxycycline concentration by tenfold (0.2 mg/ml), as well as decreased the treatment duration, which started only after pups were born rather than during pregnancy. However, although we found that GCaMP expression levels were adequate in L<sub>4</sub>, expression in L<sub>2/3</sub> was sparse and labeled at most only tens of cells, as opposed to hundreds within a typical imaging field of view. The final cohort of mice received doxycycline diluted another tenfold (0.04 mg/ml) for a similar duration of time as the previous group. Although GCaMP expression levels across layers were reasonable, after conducting the same visual tuning experiments as described above, we found the same type of correlational structure we had previously observed in the CaMKII-tTA;tetO-GCaMP6s mice without doxycycline treatment. In summary, under the conditions tested, we were either unable to have GCaMP expression levels high enough across cortical layers to be usable for imaging, or expression was adequate but we were unable to eliminate the presence of neurons with highly correlated signal and noise correlations. In addition, due to the long timescale of testing—months for each iteration—we ultimately chose to pursue a different approach for labeling L<sub>4</sub> neurons in V1.

#### 2.4 SETUP FOR SINGLE-NEURON PHOTOSTIMULATION EXPERIMENTS

We used the L<sub>4</sub>-specific Scnn1a-Tg3-Cre mouse line (Madisen et al., 2010) to label excitatory neurons in L<sub>4</sub> (Figure 2.2a). We used Cre-dependent adeno-associated viral vectors to co-express the calcium indicator jGCaMP7f (Dana et al., 2019) and soma-localized ChRmine, a sensitive red-shifted channelrhodopsin (Marshall et al., 2019), to be able to perform simultaneous calcium imaging and two-photon photostimulation, respectively, within L<sub>4</sub> (Figure 2.2c). Retinotopic

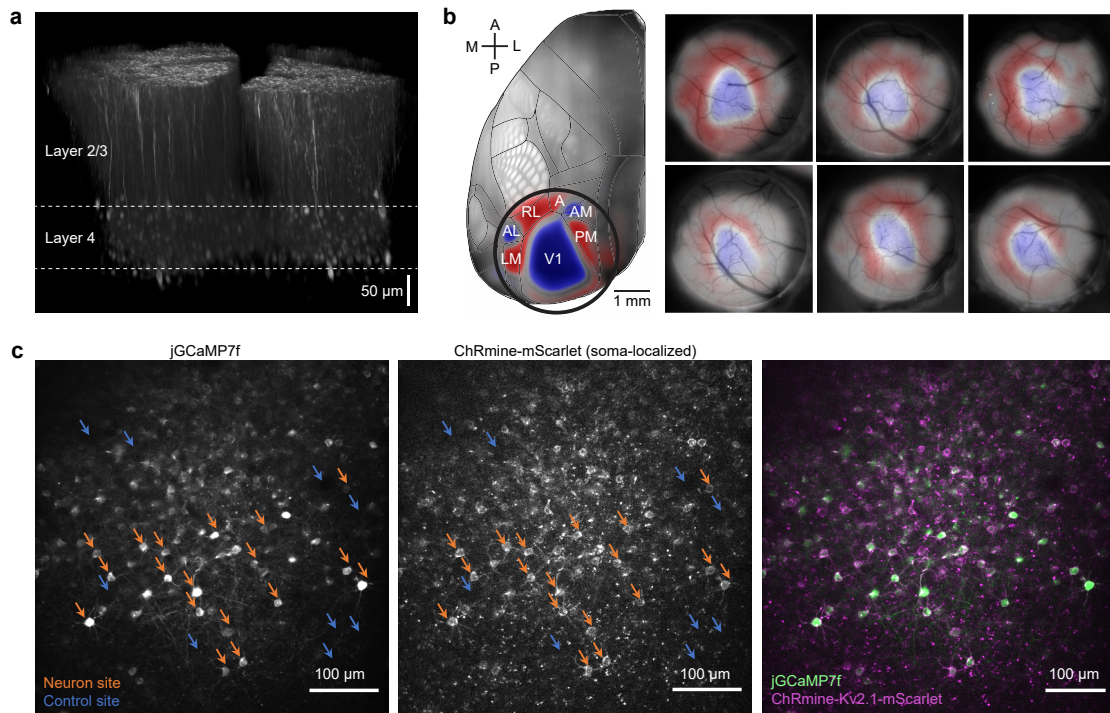


**Figure 2.2: Labeling strategy for L4 single-neuron photostimulation experiments.** **a**, 3D stack, coronal view of V1 in an *Scnn1a-Tg3-Cre* mouse expressing eGFP in L4 excitatory neurons. **b**, Left, top surface view of cortex (left, lateral; right, medial; top, anterior; bottom, posterior) template showing mean field sign map ( $n = 79$  mice) and area parcellation, from the Allen Institute. Circle shows positioning of 3.5 mm cranial window used for experiments. Right, field sign retinotopic maps overlaid on vasculature from 6 example mice. Blue regions denote V1 and areas with highest expression, from which experimental fields of view were chosen. **c**, Images of example field of view in L4, with orange and blue arrows denoting neuron and control photostimulation sites, respectively. Left, jGCaMP7f expression. Middle, soma-localized ChRmine tagged with mScarlet. Right, overlay of jGCaMP7f (green) and ChRmine (magenta) expression.



maps were collected prior to beginning experiments to inform what portion of  $V_I$  was being imaged for each session (Figure 2.2b).

We built a custom microscope that contains two independent scan paths, one for two-photon photostimulation and another for two-photon imaging (Figure 2.4). The photostimulation path contained a pair of galvanometric mirrors for beam steering. We considered multiple configurations for photostimulation and chose to use a scanning-based approach for a number of reasons: rapidly scanning a nearly diffraction-limited spot in a spiral-like pattern over each neuron (Chetih and Harvey, 2019; Packer et al., 2012; Yang et al., 2018) is straightforward to implement and has improved resolution (Rickgauer and Tank, 2009), works well to drive action potentials relatively quickly in potent opsins such as ChRmine (Marshel et al., 2019), used here, and requires less average laser power than scanless holographic approaches (Yang et al., 2018), reducing concerns about heat-induced effects on cell health (Podgorski and Ranganathan, 2016). In comparison, holography uses refocusing of the beam into a soma-sized spot, which degrades axial resolution but can be compensated for using temporal focusing (Oron et al., 2005; Papagiakoumou et al., 2020; Pégard et al., 2017; Zhu et al., 2005), although this methodology is more involved and requires additional optical components.

To further try and maximize photostimulation resolution, we used viral constructs that included soma-targeting sequences (such as  $Kv2.1$ ) to enhance opsin expression at the soma and minimize expression in other cell compartments, which have been shown to reduce off-target stimulation of axons or dendrites of other neurons (Baker et al., 2016; Lim et al., 2000; Marshel et al., 2019). We also attempted to use lower laser powers for photostimulation such that neurons could be reliably activated and without excess activation failures. With the photostimulation conditions

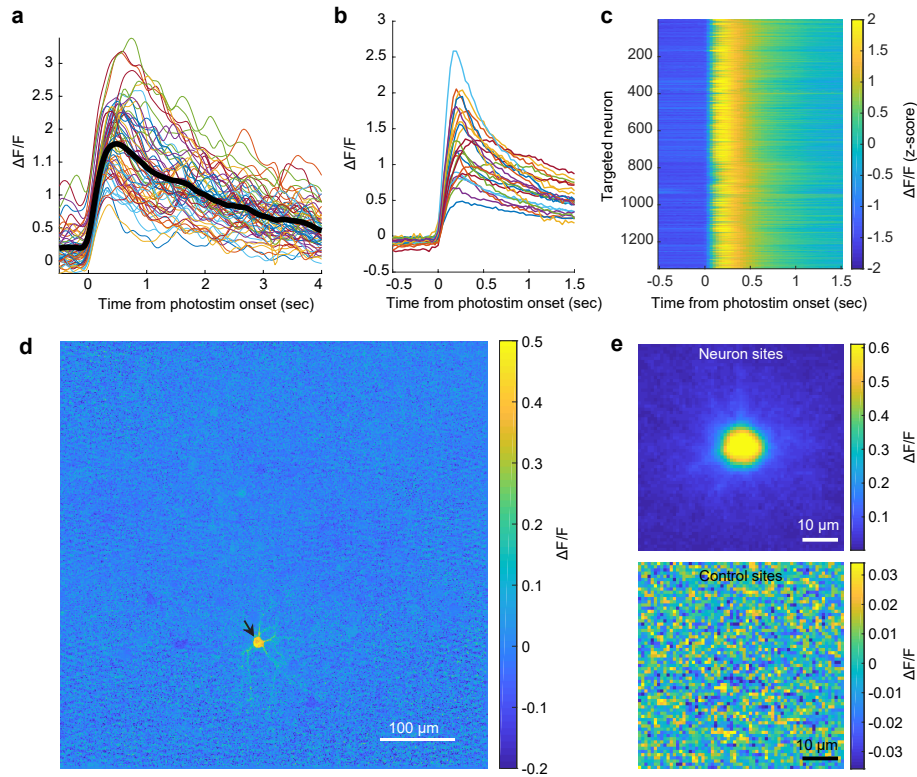


**Figure 2.3: Photostimulation responses of targeted sites.** **a**, Single-trial responses (colored lines, smoothed for visualization) and mean response (black line) for an example targeted neuron ( $n = 180$  trials). **b**, Photostimulation responses averaged over trials ( $n = 180$ ) for all targeted neurons ( $n = 25$ ) in one example session. Note that all neurons increase their activity in response to stimulation. **c**, Trial-averaged photostimulation responses for significantly photostimulated targeted neurons across all sessions ( $n = 1,345$  of 1,398 total neurons; 96.2% significantly responsive to stimulation). **d**, Photostimulation-triggered average fluorescence image for a single targeted neuron, with black arrow indicating photostimulation target location. **e**, Photostimulation-triggered average fluorescence images centered on either target ( $n = 25$ ) or control sites ( $n = 5$ ),  $n = 180$  trials per site.

used, opsin-expressing neurons in L<sub>4</sub> of V<sub>1</sub> in awake mice reliably responded to photostimulation on individual trials (Figure 2.3a), with nearly all neurons being responsive to photostimulation when responses were averaged over all stimulation trials (Figure 2.3b, c). To check the resolution of stimulation, we also computed photostimulation-triggered average (PTA) fluorescence images for each targeted site. If the resolution is poor, we would expect that the PTA images would show diffuse activation of neurons both centered at and adjacent to the targeted location, whereas if the resolution is good, we would expect to see higher fluorescence in the shape of a cell with a sharp outline at the center targeted site. We confirmed that photostimulation induced cell-shaped increases in fluorescence at the targeted site, but not at control sites where we targeted regions that lacked opsin expression, which we used to account for effects as a result of non-specific photostimulation laterally or axially (Figure 2.3d-e). Thus, we concluded that we were able to photostimulate neurons with reasonable resolution, although this could be further improved with alternative viral approaches to restrict opsin expression to a sparser subset of L<sub>4</sub> neurons.

## 2.5 METHODS

### 2.5.1 ANIMALS AND SURGERY

All experimental procedures were approved by the Harvard Medical School Institutional Animal Care and Use Committee (IACUC).

Scnn1a-Tg3-Cre mice used in experiments were generated by mating male Scnn1a-Tg3-Cre mice with female C57BL/6J mice, obtained from The Jackson Laboratory (C57BL/6J, stock number 000664; Scnn1a-Tg3-Cre, stock number 009613) and genotyped by Transnetyx. Mice were

housed at 65–75 °F with 35–65% humidity and on a 12-h reverse light/dark cycle. Mice were used for imaging experiments between 3 and 6 months of age. Prior to imaging, mice underwent surgery to implant a chronic cranial window and headplate. Mice were injected intraperitoneally with dexamethasone (3 µg per g body weight) 3–6 h before surgery to reduce brain swelling. During surgery, mice were stably anesthetized with isoflurane (1–2% in air). A titanium headplate was attached to the skull using dental cement (C&B Metabond, Parkell). A ~3.5-mm diameter craniotomy was made over left V1 (stereotaxic coordinates: 2.5 mm lateral, 3.4 mm posterior to bregma). A virus mixture of AAV9-syn-FLEX-jGCaMP7f-WPRE (Addgene 104492, Dana et al., 2019) and either channelrhodopsin construct of AAV9-CAG-DIO-ChRmine-mScarlet-Kv2.1-WPRE-hGH or AAV9-hSyn-DIO-ChRmine-mScarlet-Kv2.1-WPRE-hGH (custom, synthesized by GenScript; virus prepared by Boston Children’s Hospital Viral Core) was diluted into phosphate-buffered saline at final titers of  $\sim 1.35 \times 10^{12}$  gc/ml and  $\sim 2 \times 10^{12}$  gc/ml, and mixed 10:1 with 0.5% Fast Green FCF dye (Sigma-Aldrich) for visualization. Virus was injected in a 3 × 3 grid with 350 µm spacing near the center of the craniotomy at 400 µm below the dura, with ~75 nl at each site. Injections were made slowly (over 2–5 min) and continuously using beveled glass pipettes and a custom air pressure injection system. The pipette was left in place for an additional 2–5 min after each injection. Following injections, the dura was removed. A glass plug consisting of two 3.5-mm coverslips and one 4.5-mm coverslip (1 thickness, Warner Instruments) glued together with UV-curable transparent optical adhesive (Norland Optics, NOA 81) was inserted into the craniotomy and cemented in place with cyanoacrylate (Insta-Cure, Bob Smith Industries) and metabond mixed with carbon powder (Sigma-Aldrich) to prevent light contamination from the visual stimulus. An aluminum ring was then cemented on top of the headplate, which interfaced with the objective lens of the microscope through black rubber light

shielding to provide additional light-proofing. Imaging datasets were collected at least 2 weeks post-surgery, and data collection was discontinued once baseline GCaMP levels and expression in nuclei appeared to be high.

### 2.5.2 VISUAL STIMULI FOR EXPERIMENTS COMPARING NEURAL ACTIVITY ACROSS MOUSE LINES

Visual stimuli were presented as described in Kafashan et al., 2021. Stimuli consisted of square-wave gratings presented on a gray background to match average luminance across stimuli. Gratings were windowed outside of a central circle of radius  $20^\circ$  with a Gaussian of  $19^\circ$  standard deviation to prevent monitor edge artifacts. Grating drift directions were pseudo-randomly sampled from  $45^\circ$  to  $360^\circ$  in  $45^\circ$  increments at 10 or 20% contrast, spatial frequency of 0.035 cycles per degree, and temporal frequency of 2 Hz. Stimuli were presented for 500 ms, followed by a 500ms gray stimulus during the inter-stimulus interval (1 Hz presentation). The visual stimulus was designed to be minimally sensitive to the small eye movements typical of mice (Keller et al., 2012; Saleem et al., 2013). In addition to using a full field grating, the stimulus presentation of 500ms and temporal frequency of 2 Hz was chosen so that each trial consisted of exactly one complete cycle. The effect of fixational eye movements was thus mostly a small shift in phase of the perceived stimulus, which should have little impact on spike counts summed over the full stimulus presentation.

### 2.5.3 WIDEFIELD RETINOTOPIC IMAGING

Retinotopic maps were collected using widefield imaging as described previously (Driscoll et al., 2017; Minderer et al., 2019). Mice were anesthetized with isoflurane (0.5–1.25% in air). A

tandem-lens epifluorescence microscope with an inverted camera lens was used to reflect filtered light onto the brain and collect emission light from GCaMP fluorescence, imaged by a second camera lens onto a CMOS camera. A spherically-corrected periodic black and white checkered moving bar was presented on a monitor positioned in front of the mouse's right eye at a 30° angle. Retinotopic maps were computed from the temporal Fourier transform of the imaging data at each pixel with the signal phase at the stimulus frequency subtracted, and then smoothed with a Gaussian filter. Field sign maps were aligned to an image of the vasculature pattern at the brain surface taken under the same field of view.

#### 2.5.4 MICROSCOPE DESIGN

Data were collected using a custom-built two-photon microscope with two independent scan paths, one for imaging and one for photostimulation, that were merged through a Nikon 16 × 0.8 NA water immersion objective (Figure 2.4). For the imaging path, a Ti:Sapphire laser (Coherent Chameleon Vision II) was used to deliver 935 nm excitation light for calcium imaging at 30 Hz, with the scan head consisting of a resonant-galvanometric scanning mirror pair separated by a scan lens-based relay. The photostimulation path used either a Fidelity-2 fiber laser (Coherent) at 1,070 nm or a custom low repetition rate (2 MHz) Spark fiber laser at 1,060 nm to deliver excitation through a galvanometric-galvanometric pathway using the same scan lens-based relay as in the imaging path. Note that the microscope contained an electrically tunable lens (ETL) in the imaging path that was conjugated to the back aperture of the objective, which allows the control current to the ETL to linearly change the focal plane in the sample space independently from the photostimulation path and therefore enables imaging in  $z$ -volumes separated by hundreds of microns (e.g., in both L4 and L2/3) nearly simultaneously (Grewe et al., 2010; Vladimirov et

al., 2018; Yang et al., 2018). The microscope also included a spatial light modulator (SLM) with sub-3 ms refresh time to generate holographic patterns in the photostimulation path, allowing for 3D stimulation, but this and the ETL were not utilized for volumetric imaging or holographic stimulation in the experiments described here. The imaging and photostimulation paths were merged before the objective with a longpass dichroic mirror with 1,000 nm cut-on (Thorlabs DMLP1000L) and co-aligned to the same focal plane by imaging a pollen sample through each pathway. Collection optics were housed in a light-tight aluminum box to prevent contamination from visual stimuli. Green and red emitted light were separated by a dichroic mirror (580 nm longpass, Semrock) and was filtered (525/50 or 641/75 nm, Semrock) and collected by GaAsP photomultiplier tubes (Hamamatsu). Microscope hardware was controlled by ScanImage 2018 (Vidrio Technologies). Rotation of the spherical treadmill along three axes was monitored by a pair of optical sensors (ADNS-9800) embedded into the treadmill support communicating with a microcontroller (Teensy, 3.1). The treadmill was mounted on an XYZ translation stage (Dover Motion) to position the mouse under the objective.

#### 2.5.5 PHOTOSTIMULATION PROTOCOL

The photostimulation protocol used either a spiral scan or log-spiral scan (Chettih and Harvey, 2019) of a diffraction-limited spot across an area similar to the size of each targeted neuron ( $\sim 10 \mu\text{m}$ ), with  $10 \times 10$ -ms spirals for a total of 100 ms stimulation. The power used for photostimulation of each neuron was typically  $\sim 6 \text{ mW}$ , but ranged from 4.5 to 12 mW.

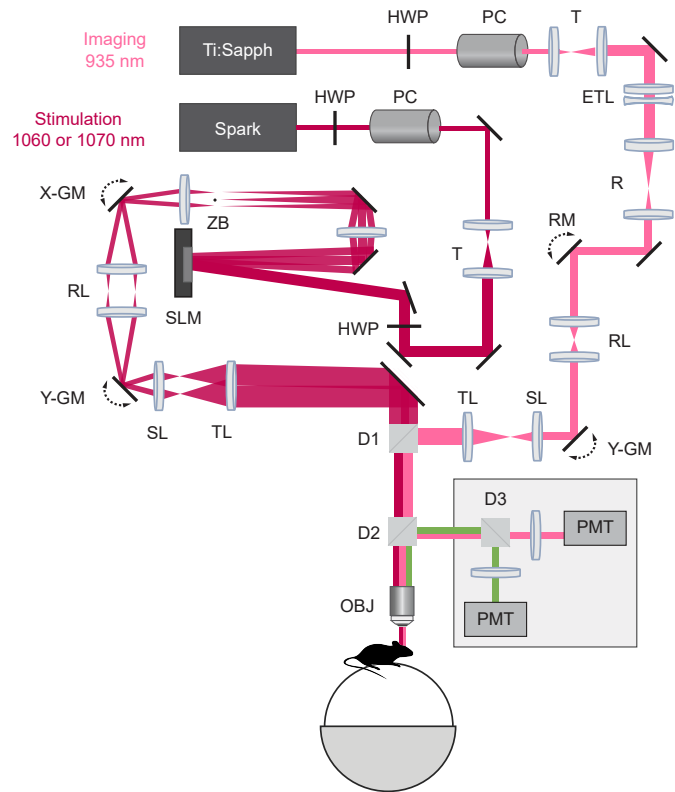


**Figure 2.4: Optical layout of the custom-built ETL- and SLM-based two-photon *in vivo* photostimulation microscope.** HWP, half-wave plate; PC, Pockels cell; T, telescope; ETL, electrically tunable lens; R, relay; RM, resonant mirror; X-GM, Y-GM, galvanometers; SL, scan lens; TL, tube lens; ZB, zero-order block; D<sub>1</sub>, D<sub>2</sub>, D<sub>3</sub>, dichroics; PMT, photomultiplier tube; OBJ, objective.



### 2.5.6 IMAGING DATA PRE-PROCESSING

Imaging frames were first motion-corrected using custom MATLAB code ([https://github.com/HarveyLab/Acquisition2P\\_class](https://github.com/HarveyLab/Acquisition2P_class)) on sub-frame, full-frame, and long (minutes to hours) timescales. Batches of 1,000 frames were corrected for rigid translation using subpixel image registration, after which frames were corrected for non-rigid warping on sub-frame timescales using a Lucas-Kanade method. Non-rigid deformation on long timescales was corrected by selecting a global alignment reference image (average of a 1000-frame batch) and aligning other batches by fitting a rigid 2D translation, followed by an affine transform and then nonlinear warping. Motion-corrected data was then input to Suite2p to extract sources and associated fluorescence traces. To classify sources, similar to previous work (Chettih and Harvey, 2019; Minderer et al., 2019), we re-trained an existing 3-layer convolutional neural network in MATLAB. Each source's spatial footprint was cropped into a  $25 \times 25$  pixel image ( $\sim 0.88 \mu\text{m}$  per pixel) as input to the network, which was constructed with 3 convolutional layers ( $5 \times 5$  filter size; numbers of filters per layer, 32, 16, 16; stride 1), a 256-unit fully connected layer, and a 2-unit softmax output layer. We used an additional 6,626 manually annotated L4 sources, further augmented 20-fold by rescaling, rotation, and reflection. Sources were classified as cell bodies or other. Only data from cell bodies were used in analyses. Predictions for an example L4 session are shown in Figure 2.5.

To obtain  $\Delta F/F$  traces, we estimated baseline fluorescence by examining the distribution of fluorescence in a two-minute window around each sample time point and normalizing by the 20th percentile value. Traces were deconvolved using the constrained AR-1 OASIS method (Friedrich et al., 2017) and individually optimized decay constants.

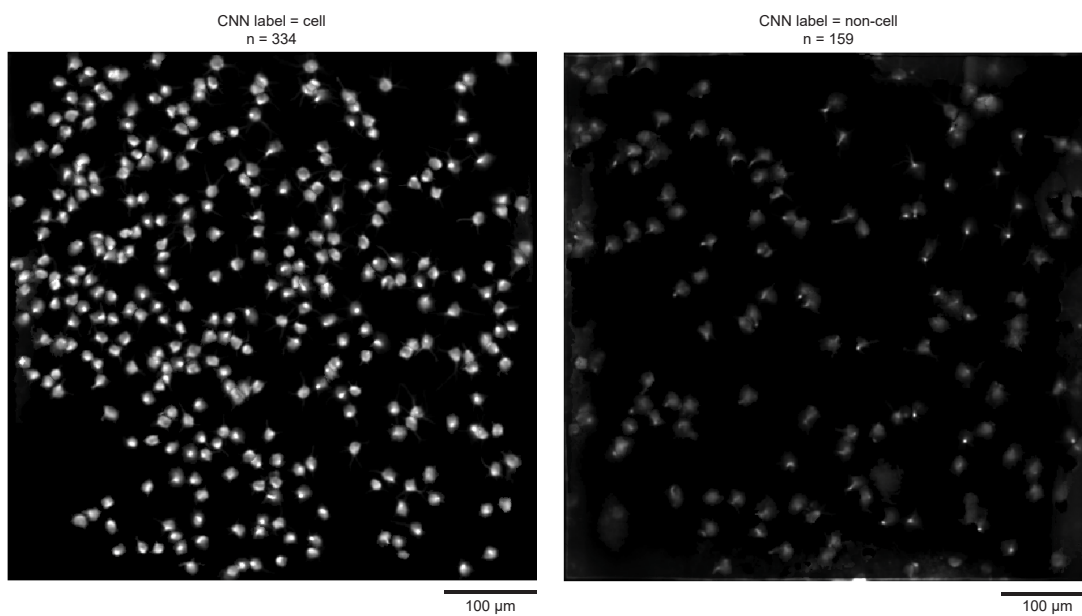


**Figure 2.5:** Sources and labels from CNN for an example L4 session. Left, cell source predictions. Right, non-cell source predictions.

# 3

## Influence Mapping Shows Signatures of Amplification in V1 L4

### 3.1 INTRODUCTION

L4 is known to be visually tuned to features such as stimulus direction and orientation (Niell and Stryker, 2008; Sun et al., 2016; de Vries et al., 2020). Previous work has shown that L4 amplifies thalamocortical inputs without altering their tuning (Li et al., 2013b; Lien and Scanziani, 2013),

suggesting that neurons form subnetworks in which recurrent excitation increases responses between cells with shared preferred stimuli. However, it has not been tested whether amplification within L<sub>4</sub> occurs via like-to-like functional motifs, and if so, whether it is feature-specific. Given the recurrent nature of cortical circuits and technical limitations with previous methods, these questions are difficult to address. This motivates using influence mapping, as it uses single-neuron perturbations that enable causal, direct estimation of functional architectures. We investigated how local circuitry within L<sub>4</sub> of V<sub>1</sub> transforms representations by photostimulating individual neurons while imaging responses of hundreds of neighboring neurons of known tuning.

### 3.2 EXPERIMENTAL DESIGN

Within each experimental session in head-fixed awake mice free to run on a styrofoam trackball, we used separate blocks to measure influence and visual tuning properties of the imaged neural population in L<sub>4</sub> of V<sub>1</sub> (Figure 3.1). We first used a short seeding block, in which 100% contrast drifting gratings were presented, to quickly visualize which neurons showed responsiveness to visual stimuli and tuning to orientation and direction. The maps generated from this block were then used in combination with online manual judgment of GCaMP and opsin co-expression levels to select neuron targets for photostimulation in subsequent blocks. In influence measurement blocks, we photostimulated individual targeted neurons or control sites, where there was lower or a lack of clear opsin expression, while imaging the responses of all neighboring neurons within the field of view. To understand influence within the context of visual processing rather than complete darkness, each photostimulation trial occurred simultaneous to the onset of low-contrast drifting grating stimuli (10% contrast, eight directions spaced 45° apart, fixed spatial fre-

quency and temporal frequency). Two separate visual tuning blocks were used. One consisted of presentation of high-contrast drifting gratings and another consisted of contrast-modulated Gaussian noise movies (see descriptions below).

### 3.2.1 MAGNITUDE OF NEURAL RESPONSES DURING EXPERIMENTAL BLOCKS

We wanted to ensure that the magnitude of responses to photostimulation were still in a reasonable range compared to the neuron's responses in the visual tuning blocks. Compared to neural activity in the influence measurement block during presentation of 10% contrast gratings without photostimulation, adding photostimulation of targeted neurons during visual stimuli resulted in greater responses. These photostimulation-evoked activity levels were slightly lower than those during the preferred stimulus in the high-contrast random gratings tuning block, and substantially lower than responses to the Gaussian noise movies (Figure 3.2). Together, these results indicated that photostimulation was able to further boost activity on top of the response to a low-contrast visual stimulus, and that the magnitude of photostimulation fell within physiological levels, as it was still lower than responses to other visual stimuli that were presented.

### 3.3 CALCULATION OF INFLUENCE

We needed to quantify how photostimulation of a given target site affected the activity of non-targeted neurons in the imaging field of view. As in previous work, we used deconvolved neural activity to calculate a  $\Delta$ Activity influence metric, which is similar to a  $z$ -score and was defined as the response of non-targeted neurons on single photostimulation trials with their average response on control trials with the same grating subtracted, and then normalized by the standard deviation of the difference over all trials (Chettih and Harvey, 2019). To get an influence value

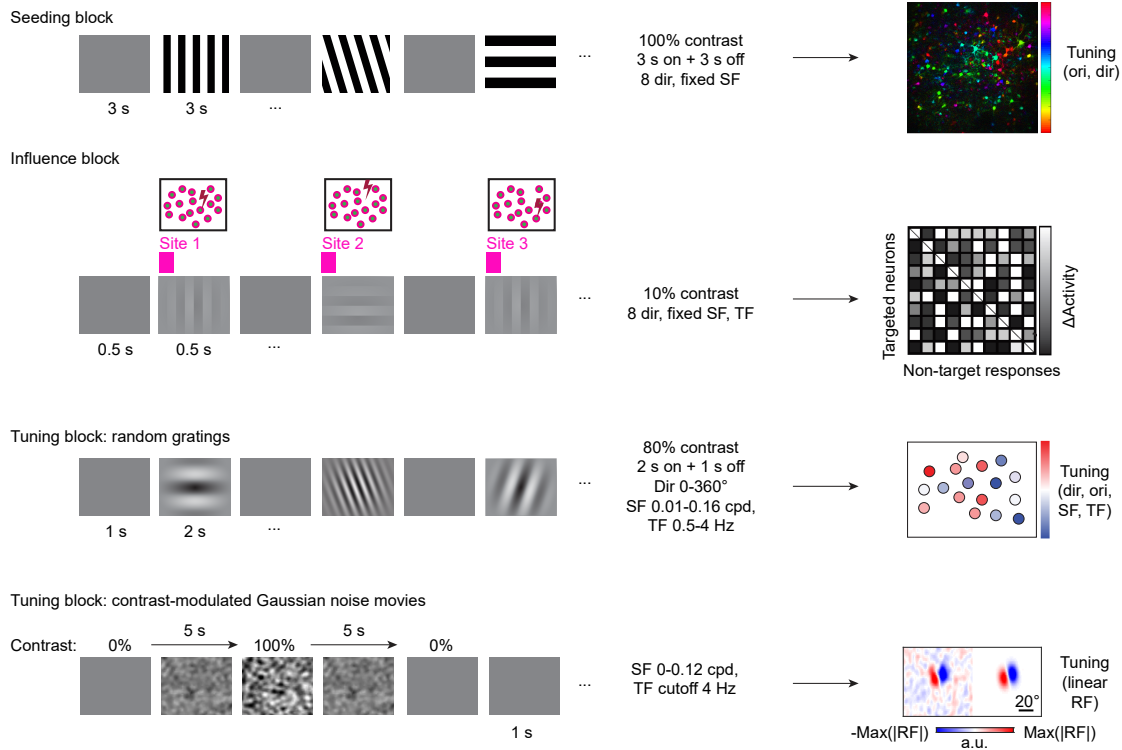


**Figure 3.1: Schematic of experimental protocol.** Top row, seeding block: high-contrast gratings used to extract orientation and direction tuning, used in combination with online judgment of GCaMP and opsin co-expression to select neuron targets for photostimulation. Second row, influence block: sites are photostimulated concurrent with low-contrast drifting gratings while imaging responses of all neurons within a given experimental session's field of view. Third row, random gratings tuning block: each visual stimulus parameter (direction, spatial frequency, temporal frequency) were randomly sampled on each trial. Responses were used to extract visual tuning properties such as direction, orientation, spatial frequency, and temporal frequency preference. Bottom row, contrast-modulated Gaussian noise movie block: the stimulus was sinusoidally contrast-modulated over 10 seconds from gray to gray, after which linear RFs were obtained by reverse correlation of neural responses to the sequence of movies (scale bars: RF, 20°; a.u., arbitrary units).

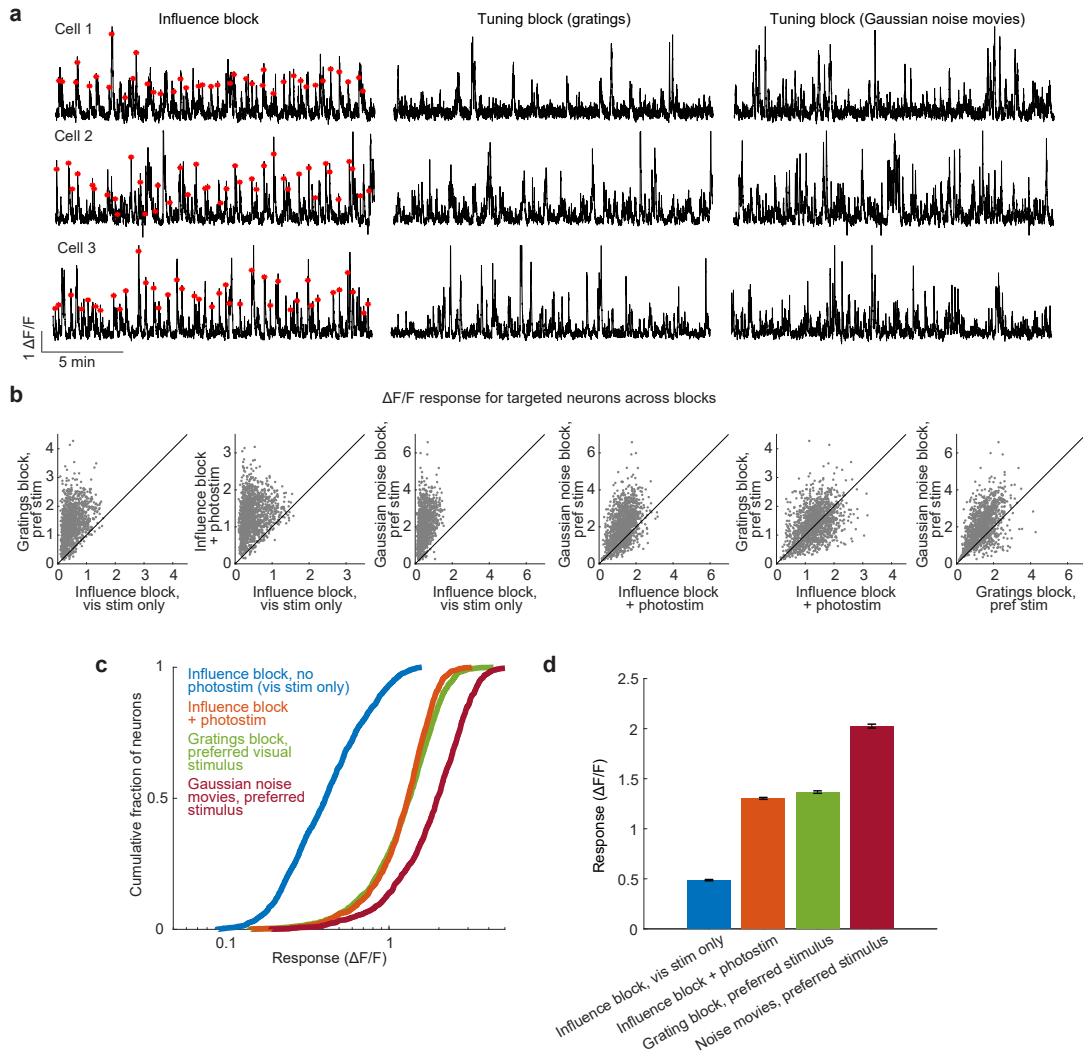


**Figure 3.2: The magnitude of V1 L4 targeted neuron responses to photostimulation and visual stimuli.** **a**, Each row shows an example cell's response during an influence block (left column), gratings tuning block (middle column), or Gaussian noise movie tuning block (right column). Red asterisks denote times at which that cell was photostimulated. **b**, Comparison of responses of individual targeted neurons ( $n = 1,345$ ) between all combinations of influence blocks with no photostimulation (visual stimulus only), influence block with photostimulation and visual stimulus, preferred stimulus in the high-contrast random gratings tuning block, or preferred stimulus in the Gaussian noise movie tuning block. **c**, Responses of targeted neurons during the influence block with visual stimulus only (blue) or with visual stimulus and photostimulation (orange), preferred visual stimulus in the gratings block (green), and preferred visual stimulus in the Gaussian noise movie block (red). Influence block with photostimulation vs. preferred visual stimulus in the tuning block, influence block with photostimulation vs. preferred visual stimulus in the Gaussian noise movie block:  $P = 0.0436$ ,  $P = 2.65 \times 10^{-107}$ , Mann-Whitney  $U$  test ( $n = 1,345$  neurons). **d**, Average targeted neuron response to each of the four conditions, as in **b-c**. Data shown as mean  $\pm$  s.e.m., calculated by bootstrap.

for each target-nontarget neuron pair, we averaged a neuron's  $\Delta$ Activity over all photostimulation trials for the target. In all influence-related analyses, we excluded target-nontarget pairs that were less than 25  $\mu\text{m}$  apart (although changing the cutoff yielded qualitatively similar results) in order to limit the effect of potential off-target photostimulation. The distribution of influence values within L<sub>4</sub> was centered near zero and included both positive and negative values (Figure 3.3a), which corresponded to excitatory and inhibitory effects, respectively.

We then visualized photostimulation-triggered average images at the locations of non-targeted neurons, split by positive or negative influence. For neurons that were positively influenced (i.e., positive  $\Delta$ Activity), we would expect to see a cell-shaped increase in fluorescence, and negative fluorescence for neurons that were negatively influenced (i.e., negative  $\Delta$ Activity). For both positive and negative influence values, we found that these indeed corresponded to cell-shaped fluorescence changes in raw images averaged over center locations of non-targeted neurons (Figure 3.3b), indicating that there was true recruitment or suppression of non-targeted neurons through photostimulation of targeted neurons. Furthermore, the absolute value of average non-targeted neuron fluorescence changes was much smaller than those of neurons directly targeted for stimulation, which is expected given that we aimed to avoid using excessively strong laser powers for photostimulation.

After visually verifying that target photostimulation induced cell-shaped changes in fluorescence at non-targeted neuron sites, we then compared influence between photostimulation of either neuron sites or control sites. Control sites were areas in the imaging field of view that either lacked or had low opsin expression, which could show whether influence could result from lateral or axial off-target photostimulation, and served as a within-session comparison against neuron



targets. Non-zero control site influence values could potentially be accounted for by dense opsin labeling in L4 neurons and off-target effects from imperfect single-cell resolution of photostimulation, as well as by the sampling of noisy or random neural activity. However, although both neuron and control sites showed negative and positive influence, influence of targeted neurons was more positive compared to that of control sites (Figure 3.3c). In addition, the magnitude of influence values was greater for neuron site photostimulation by  $\sim 4\%$  (Figure 3.3d). When examining the signed mean influence in neuron versus control site stimulation, the positive mean bias indicated that this effect was in part driven by neuron targets positively influencing other neurons, whereas control site photostimulation influence was of mixed sign and therefore was approximately zero (Figure 3.3e). Furthermore, the standard deviation of influence values from neuron sites was greater by  $\sim 9\%$  than that of control sites (Figure 3.3f). This result would be expected if stimulation of targeted neurons consistently recruited other neurons with specific properties, which should then show a greater spread of influence value variability compared to if noise was being sampled instead, as would be expected during control site photostimulation. Together, these observations provide evidence that there was measurable influence from photostimulating L4 neurons. Furthermore, the greater dispersion in influence values from neuron site photostimulation suggested that there could be structure to this influence, which may be related to properties of the target-nontarget neuron pairs.

We next analyzed influence with respect to the anatomical distance between target-nontarget neuron pairs. Influence varied as a function of distance (Figure 3.3g). Net influence was strongly excitatory compared to control for neurons that were less than 100  $\mu\text{m}$  apart. In more intermediate distances through 450  $\mu\text{m}$ , influence was slightly negative, although the relative magnitude was much smaller than that of the local excitatory influence. At the longest distances of >450  $\mu\text{m}$  to  $\sim$ 550  $\mu\text{m}$ , net influence was near zero. Control site influence showed a similar but weaker spatial structure, consistent with potential effects from off-target stimulation. Furthermore, in line with this idea, when we performed a median split of neuron site influence by the magnitude of the photostimulated neuron, we found that the influence–distance relationship for targeted sites that were more weakly photostimulated was left-shifted towards the curve for control site stimulation (Figure 3.3h). We concluded that the distance between a target and non-target neuron pair was a factor that contributed to influence, especially at shorter distances.

### 3.4 TUNING WITHIN L4

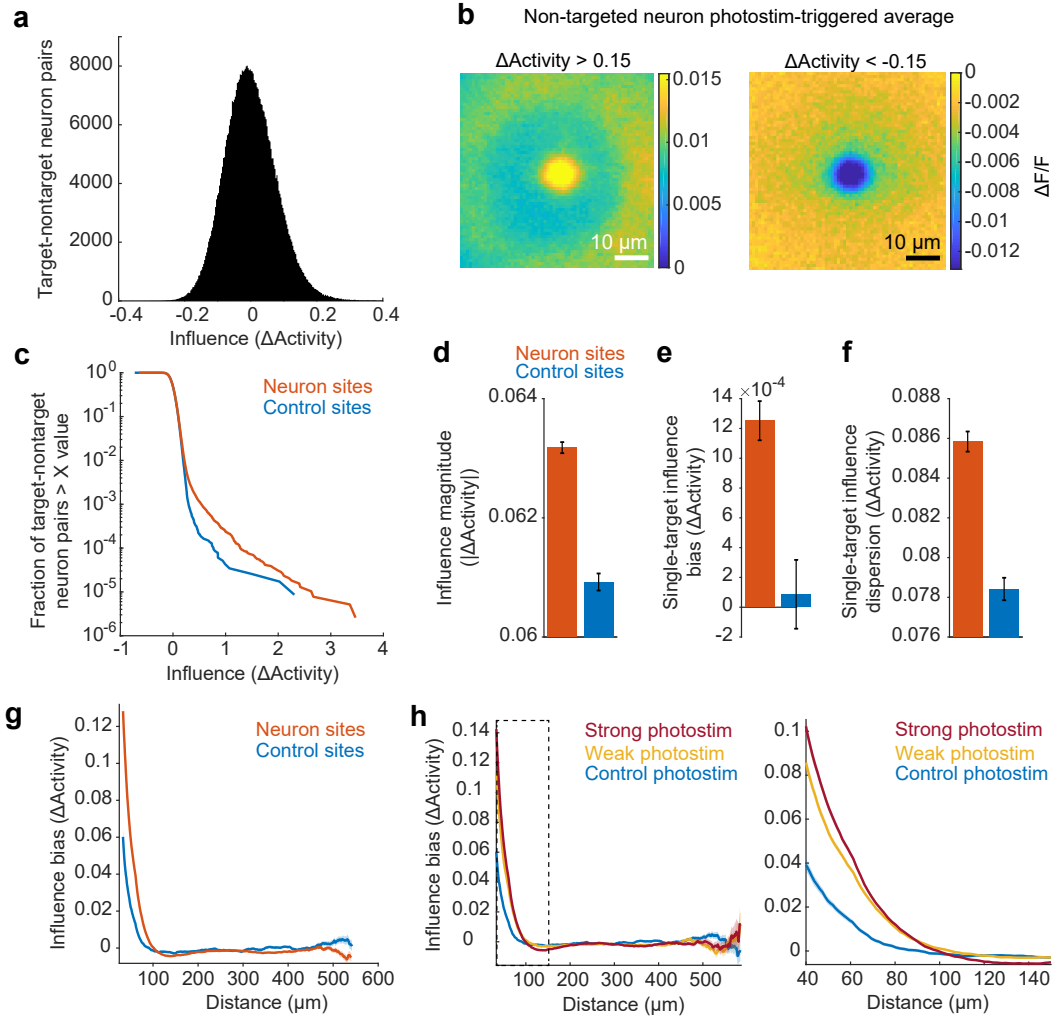
After quantifying influence, we then sought to test whether neurons with similar tuning amplify each other’s activity by characterizing visual tuning of L4 V1 neurons, in order to relate influence to functional properties in the same cells. We used two different sets of stimuli, drifting gratings and Gaussian noise movies, to probe visual tuning of the recorded neurons.

#### 3.4.1 RANDOM GRATINGS TUNING AND GAUSSIAN PROCESS REGRESSION

If sampling widely within a range of possible values for parameters of a drifting gratings visual stimulus, using the conventional method of showing many stimulus repeats is infeasible due to the number of possible combinations and the corresponding amount of increased experimen-

**Figure 3.3 (following page): Influence characterization in L4.** **a**, Distribution of influence ( $\Delta\text{Activity}$ ) values across all target-nontarget neuron and control pairs ( $n = 502,858$  pairs). **b**, Photostimulation-triggered fluorescence images, centered at all non-targeted neuron locations for target-nontarget pairs with  $\Delta\text{Activity} > 0.15$  (left;  $n = 17,006$ ) or  $\Delta\text{Activity} < -0.15$  (right;  $n = 8,814$ ). The additional halo in the excitatory non-targeted PTA may be due to dense labeling of neurons and strong local influence over multiple non-targeted neurons. **c**, Fraction of target-non-target pairs with an influence value greater than each x-axis influence value, for neuron sites ( $n = 386,799$ ) and control sites ( $n = 116,059$ ). **d**, Influence magnitude ( $|\Delta\text{Activity}|$ ) of photostimulation for all neuron target sites ( $n = 386,799$ ) or control sites ( $n = 116,059$ ). Non-zero influence magnitude is expected for control sites due to dense opsin labeling in L4 neurons and potential off-target effects, as well as random sampling of neural activity on control site photostimulation trials. Data shown as mean  $\pm$  s.e.m. calculated by bootstrap. Neuron sites vs. control sites:  $P = 5.7040 \times 10^{-4}$ , Kolmogorov–Smirnov test. **e**, Single-target influence bias is the average of signed  $\Delta\text{Activity}$  values across all non-targeted neurons. Data shown as mean  $\pm$  s.e.m. calculated by bootstrap across all neuron ( $n = 1,345$ ) or control target sites ( $n = 400$ ).  $P = 0.0870$ , Kolmogorov–Smirnov test. **f**, Single-target influence dispersion is the standard deviation of  $\Delta\text{Activity}$  across all non-targeted neurons for each individual target.  $P = 6.9298 \times 10^{-16}$ , Kolmogorov–Smirnov test. **g**, Influence bias ( $\Delta\text{Activity}$ ) versus anatomical distance between pairs of targeted neuron photostimulation and non-targeted neurons, for neuron ( $n = 386,799$ ) versus control ( $n = 116,059$ ) sites. Shading is mean  $\pm$  s.e.m. calculated by bootstrap, using a bin half-width of  $30 \mu\text{m}$ . **h**, Left: influence bias ( $\Delta\text{Activity}$ ) versus distance, as in **g**, with data from influence from neuron target sites split into stronger versus weaker responses to direct photostimulation, using a median split of photostimulation significance. For strong versus weak photostimulation groups, the mean response over targeted neurons was  $0.65 \Delta\text{F}/\text{F}$  or  $1.5 \Delta\text{F}/\text{F}$ , respectively. Dashed-line box denotes zoomed-in region, as displayed on the right panel. Note that the influence versus distance dependence for weakly photostimulated target neurons is shifted towards the control photostimulation curve, consistent with reduced but not non-zero activation when targeting control sites, which can occur from factors such as brain motion or suboptimal photostimulation resolution.

Figure 3.3: (continued)



tal time. Therefore, in one experimental block without photostimulation within each session, we presented high-contrast drifting gratings with randomly sampled drift direction, spatial frequency, and temporal frequency over a given range for each feature. We then used Gaussian process (GP) regression, a Bayesian nonparametric smoothing method, to estimate neural responses to our visual stimulus that did not contain repeats (Figure 3.4, Figure 3.5). GP regression estimates the responses by generating a high-dimensional distribution under the assumption that neural activity is a smooth function across trials with similar stimulus parameters. From the resulting fitted model, a 1D tuning curve can then be extracted for each visual feature dimension. For an example pair of a target and non-targeted neuron, visualizing two dimensions of drift direction and spatial frequency, with each dot representing one trial and colored by the magnitude of the response, we see that the GP model prediction does well at capturing the data (Figure 3.4a), and the corresponding tuning curves for each dimension from the resulting model fits can be seen (Figure 3.4b). Tuning similarity, or signal correlation, between neurons was computed as the correlation between single-trial GP predictions of the visual response for each neuron. Similarity in trial to trial variability, or noise correlations, between neurons was computed as the correlation between residuals of single trials after GP predictions were subtracted (Figure 3.4c).

GP model fit quality was distributed and fairly uniform over the field of view for each imaging experiment (Figure 3.5a). We compared GP model prediction quality on training data and on held-out data to check for the presence of overfitting, which we did not observe given that the majority of neurons fell along the unity line (Figure 3.5b). To determine how significantly a neuron was tuned to a particular stimulus dimension, we used its tuning curve and the variance of the GP model's posterior distribution over tuning values to compute a depth of modulation (DOM) index, where larger values indicate stronger tuning. The distributions of DOM were different

for the tuning dimensions of direction, spatial frequency, temporal frequency, and the mouse's running speed (Figure 3.5c). A subset of neurons showed no drift direction modulation, with many others with appreciable modulation  $>5$ . A majority of neurons showed spatial frequency modulation, whereas many neurons were not modulated by temporal frequency. As would be expected from literature linking running speed to modulation of  $V_1$  activity and depolarizing membrane potential across layers in mice (Ayaz et al., 2013; Niell and Stryker, 2010; Polack et al., 2013; Saleem et al., 2013), many neurons exhibited moderate modulation to the animal's running speed, although a large fraction of neurons also showed no or low modulation. Similar to the DOM distributions, the distribution of tuning curves of neurons significantly tuned to each dimension were also varied across features, with tuning differentially tiling the ranges of values (Figure 3.5d). Neurons showed strong orientation and direction tuning over all drift directions, with greater representation at the cardinal directions. Spatial frequency tuning was distributed over the entire range of the frequencies tested in the gratings stimulus set. Temporal frequency tuning was concentrated in the lowest and highest frequencies presented. Running speed tuning was distributed over the full range of running speeds, with a subset of neurons more concentrated at stillness or the lowest and highest speeds, and with a large subset that showed wider tuning curves over a range of intermediate to faster speeds.

### 3.4.2 GAUSSIAN NOISE MOVIES AND RECEPTIVE FIELD MEASUREMENT

In addition to measuring tuning features such as orientation, direction, spatial frequency, and temporal frequency using drifting gratings, we also were interested in understanding how visual feature preference from receptive fields (RFs), which includes attributes such as retinotopic position, could be related to influence in  $L_4$ . To measure linear RFs, we generated stochastic Gaus-

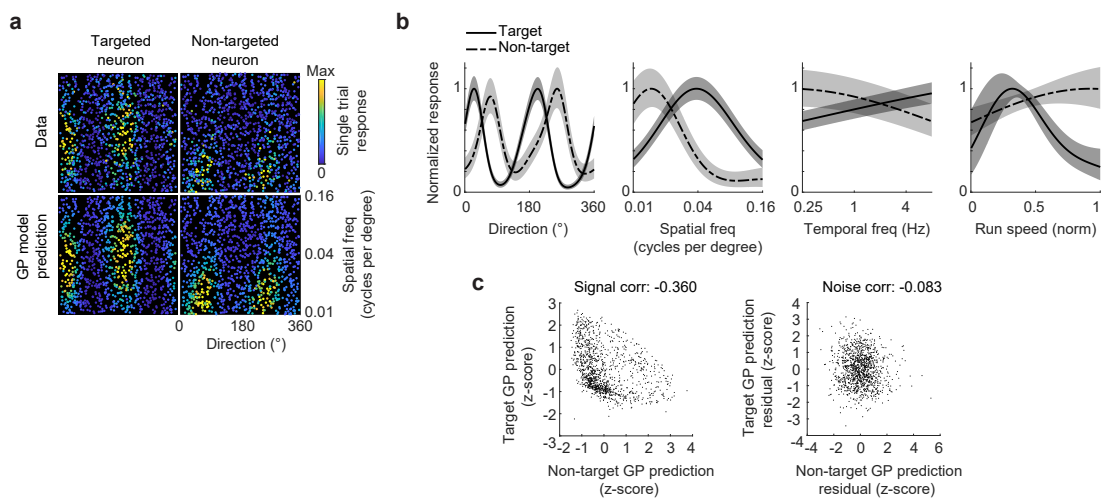


**Figure 3.4: Example tuning and activity characterization of L4 neurons using Gaussian processes.** **a**, For a pair of a targeted and non-targeted neuron (as defined by the separate influence experimental block), tuning for spatial frequency and grating drift direction. Each point is a single trial, with color indicating the mean activity throughout the duration of the visual stimulus on that trial. GP model predictions on held-out trials (bottom row) were consistent with the actual data (top row). **b**, Tuning curves from GP predictions for the targeted and non-targeted neuron in **a**. **c**, Signal correlation (left) and noise correlation (right) for the neuron pair in **a** and **b**.

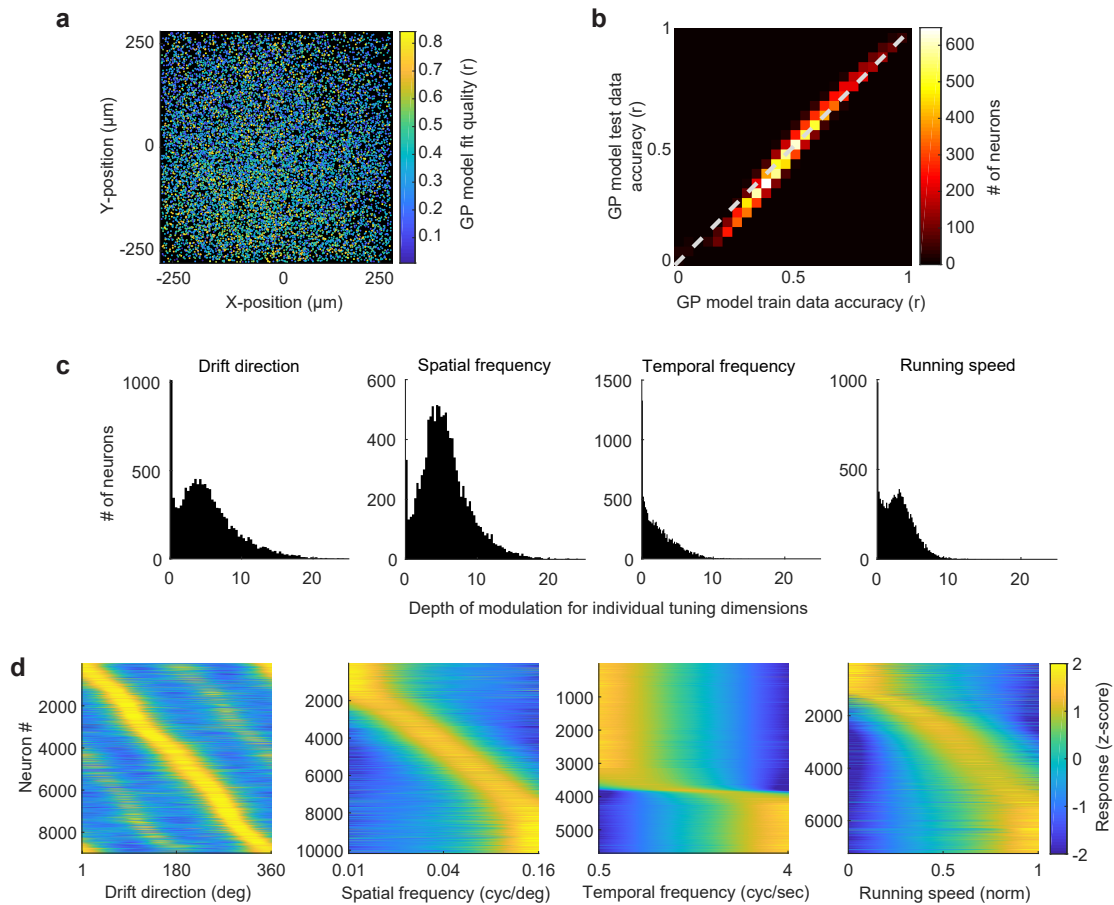


**Figure 3.5: Characterization of V1 L4 tuning using GP regression.** **a**, Position of each recorded neuron relative to the field of view of each experiment, color-coded by GP model fit quality (Pearson correlation with held-out data). Fit quality was similar across all positions. **b**, Density heatmap of GP model prediction quality (on training data; “train data accuracy”) and fit quality (on held-out data; “test data accuracy”). Most data lie on the unity line, indicating the model is not overfitting to the training data and is able to make good predictions on test data. **c**, Distributions of the DOM, or tuning significance (see Methods), for all neurons passing model fit criteria for each individual tuning dimension of gratings drift direction, spatial frequency, temporal frequency, or the animal’s running speed. Each dimension showed different distribution shapes. **d**, Tuning curves (z-scored) for each tuning dimension for neurons that passed model fit criteria and were significantly modulated (DOM > 2) for that dimension. Tuning properties were distinct for each dimension.



sian noise movies with defined spatiotemporal frequency spectra, which are a dense but structured visual stimulus that have been shown to robustly induce neural responses across layers of V<sub>1</sub> (Niell and Stryker, 2008). The movies were contrast-modulated from a gray background to full-contrast and back again over a 10 second period, in order to try and counteract habituation of neural responses and maintain high firing rates over the course of the tuning block. We calculated the spike-triggered average (STA), or reverse correlation, from the noise movies and spike trains of deconvolved activity for each neuron to extract RFs (Chichilnisky, 2001; Jones and Palmer, 1987; Niell and Stryker, 2008), which were highly diverse within the imaged population, as expected (Bonin et al., 2011; Cossell et al., 2015; Niell and Stryker, 2008; Smith and Häusser, 2010). Note that because the noise movies were limited in spatial frequency, residual noise in the STA RFs was also frequency-limited and thus showed a speckled-like appearance similar to that of the movies.

We fitted Gabor functions to parameterize the raw STAs (Figure 3.6a). For all subsequent analyses, Gabors (also referred to as “RFs” or “linear RFs”) rather than the raw STA images were used unless otherwise stated. For these analyses, only neurons with both a significant raw STA and fitted Gabor that passed a threshold for spatial correlation with the raw STA were used (see Methods). From the Gabors, in addition to the x- and y-coordinates of the center, the relative position of ON and OFF subfields were extracted (Figure 3.6b). From the subfields, we calculated an overlap metric for ON, OFF, ON+OFF subfields, or a single field (i.e., the combination of ON and OFF subfields into one merged subfield) between pairs of neurons (Figure 3.6c). We quantified similarity between pairs of RFs as the pixel-to-pixel Pearson’s correlation coefficient between the fitted Gabors. The majority of spatial RF correlations between target-nontarget neuron pairs were close to zero, with far fewer pairs showing highly correlated or anti-correlated RFs (Figure

3.6d). When examining RF similarity split by different types of subfield overlap, RF correlation was positively related to the degree of ON, OFF, and ON+OFF subfield overlap ( $R = 0.60$ ,  $R = 0.49$ ,  $R = 0.76$ ; Figure 3.6e), but not single-field overlap ( $R = 0.04$ ), as would be expected given that there are pairs with both highly correlated and anti-correlated RFs, which would show a V-shaped relationship between overlap and RF correlation.

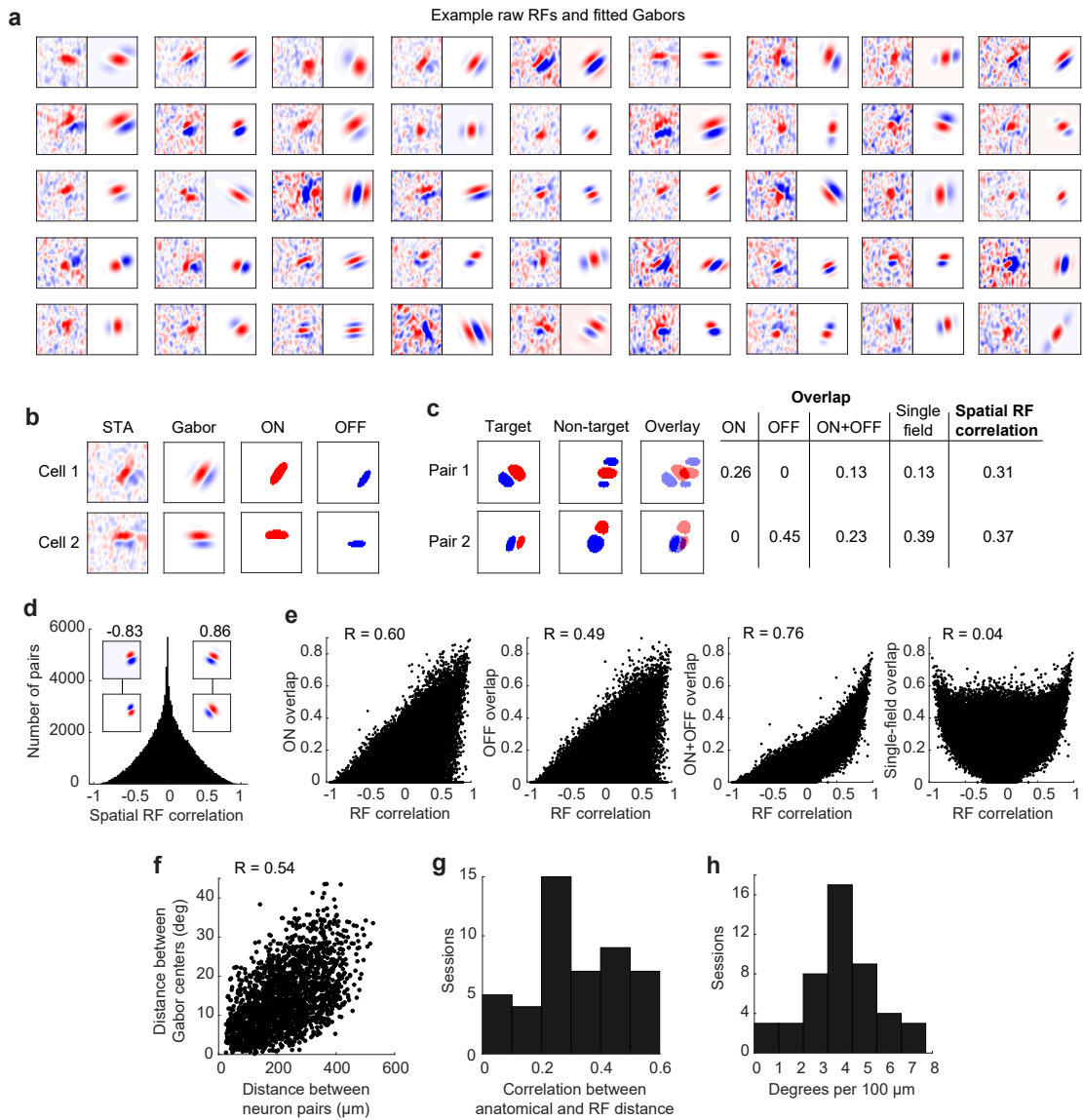
As an additional check of the STAs that were computed and the resulting Gabor fits, we verified that there was a positive relationship between the distance separating neuron pairs in anatomical space and the distance between their Gabor centers, as would be expected given the retinotopic organization of V1 (Figure 3.6f, g). The amount of RF overlap between neuron pairs also decayed with greater anatomical distances (ON overlap,  $R = -0.11$ ; OFF overlap,  $R = -0.11$ ; ON+OFF overlap,  $R = -0.17$ ; data not shown), which follows naturally from increased distance between RF centers in neurons that are farther apart in space (Bonin et al., 2011). We also estimated cortical magnification, which has been reported to be  $\sim 6-10$  degrees/100  $\mu\text{m}$  in azimuth and  $\sim 4-5$  degrees/100  $\mu\text{m}$  in elevation (Billeh et al., 2019; Bonin et al., 2011; Kalatsky and Stryker, 2003), as the slope of a linear regression model fit to Gabor center distance versus cortical distance between pairs and confirmed that the values were within expected ranges (Figure 3.6h).

### 3.5 INFLUENCE REGRESSION

To understand how the metrics described above—anatomical distance, signal and noise correlations, tuning, and RF-related properties—related to influence, we used two different approaches. For visualization purposes, we computed influence as a function of individual metrics (Figure 3.7f-l). Because metrics were correlated with each other, such as stronger influence at shorter anatomical distances between neuron pairs (Figure 3.3g) and the positive relationship between signal and noise correlations (Figure 3.7a, b), we also used a multiple linear regression-based approach to dissociate the contributions of each predictor to influence in a principled manner. The regression coefficients describe the relationship of each predictor with influence while holding the other variables constant. A positive or negative coefficient for a given predictor shows the directionality of its correlation with influence, and the magnitude describes the strength of that relationship. We also used interaction terms between activity metrics and distance to capture nonlinear effects (e.g., differences in relationships between influence and metrics at varying distances between neurons).

**Figure 3.6 (following page): Gaussian noise movies and linear RF characterization.** **a**, Raw STA RFs and fitted Gabors for an example experimental session in L4. Only significant RFs and Gabors with correlation  $>0.3$  with raw STA shown. **b**, For two example cells, the raw STA, fitted Gabor, and extracted ON (red) and OFF (blue) subregions are shown. **c**, For two example pairs of targeted and non-targeted neurons, the fitted Gabors and overlay are shown, along with the corresponding overlap metrics for ON, OFF, ON+OFF, and single-field subfields, as well as the pixel-to-pixel Pearson's correlation between RFs ("spatial correlation"). **d**, Distribution of spatial RF correlations between all L4 target-nontarget neuron pairs across experiments. Inset, example Gabors for two pairs of targeted and non-targeted neurons, with their correlation coefficients. Pairs with negative correlations typically showed similar overlap and orientation, but with reversed phase preference (i.e., swapped ON and OFF subfield locations). **e**, Relationship between RF similarity and subfield overlap metrics. The amount of ON, OFF, and ON+OFF subfield overlap (see Methods) between target-nontarget neuron pairs was strongly correlated to the RF similarity, as measured by the pixel-to-pixel correlation (ON:  $R = 0.60$ ; OFF:  $R = 0.49$ ; ON+OFF:  $R = 0.76$ ), whereas single-field overlap is not, as expected (single-field:  $R = 0.04$ ). **f**, Distance between the center of fitted Gabors (in degrees) versus distance between cell centers in anatomical space ( $\mu\text{m}$ ) for all target-nontarget neuron pairs ( $n = 2,388$ ) passing fit criteria in an example session;  $R = 0.54$ . **g**, Distribution of correlation coefficients between anatomical and retinotopic distance between target-nontarget neuron pairs for each session, shown for sessions with  $>100$  pairs ( $n = 47$ ), median  $R = 0.30$ . **h**, Calculation of visual field representation (in degrees) as a function of cortical space, using slope from a linear regression model for each experimental session (as in **f**). Median slope =  $4.0^\circ/100 \mu\text{m}$ , comparable to previous reports.

Figure 3.6: (continued)



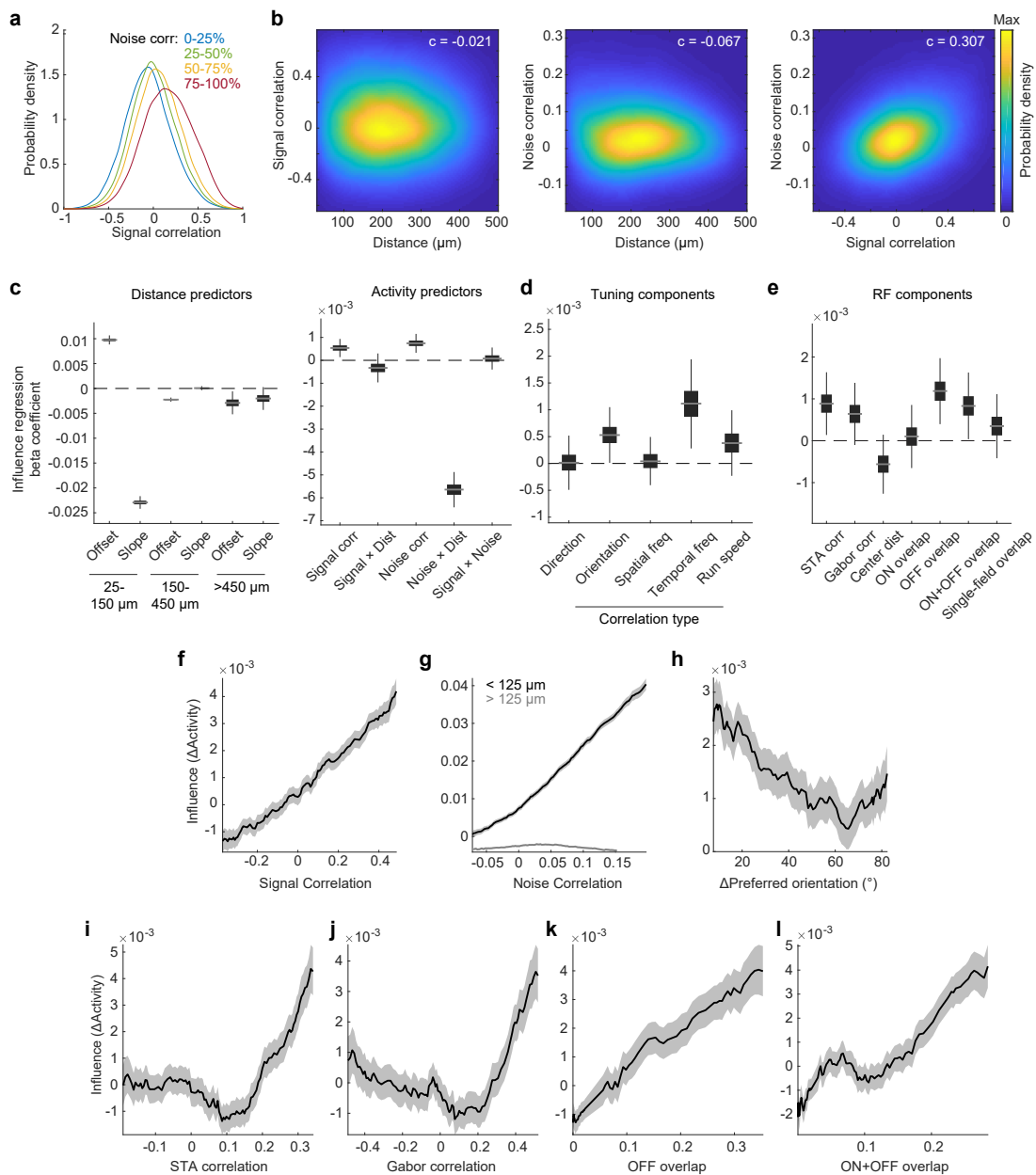
For distance predictors, influence regression showed that neuron pairs that were closer together ( $<150 \mu\text{m}$ ) had a negative slope with a positive offset, and intermediate and long-range pairs had a slope near zero with a slightly negative offset that was much smaller in magnitude compared to that of nearby pairs (Figure 3.7c). This result was consistent with the results for influence and distance described earlier, where there was a strong local excitatory relationship with influence between neuron pairs at closer distances that fell off when neurons were farther apart (Figure 3.3g).

Although common inputs are believed to be a primary source of shared variability between neurons, it is still relatively unclear whether noise correlations can also emerge from recurrent dynamics of local circuitry. From the regression analysis, noise correlations showed a positive relationship with influence at short distances, but the interaction term between noise correlations and distance was negative, which indicated that this relationship was not present at greater distances between neuron pairs (Figure 3.7c, right; Figure 3.7g). Across these short distances, noise correlations are therefore driven not only by shared external inputs over a more spatially global level, but also arise from the connectivity of local cortical networks (Malina et al., 2016; Rosenbaum et al., 2017).

If the sign of the coefficient for signal correlation is non-negative, there are two main interpretations. A positive relationship between signal correlation and influence would provide evidence for the presence of feature amplification within L4, indicating that neurons with similar activity profiles tend to excite one another. If this relationship is present only at shorter distances between neuron pairs, then this could be attributed in part to greater RF overlap between neurons located in closer lateral proximity. Alternatively, a negative coefficient would support feature competi-

**Figure 3.7 (following page): Relationship between cortical distance, activity metrics, tuning components, RF components, and influence.** **a**, Probability density function, estimated by kernel smoothing for signal correlation, for all data used in influence regression ( $n = 264,182$  pairs). Pairs were split by noise correlation quartiles and separate densities were estimated for each group. Signal correlations for neuron pairs of varying noise correlations were largely overlapping, but distinct (e.g., signal correlations for pairs with high noise correlations were right-shifted relative to pairs with lower noise correlations). These relationships between signal and noise correlations motivate using a regression approach to separate their contributions to influence. **b**, Two-dimensional probability density functions for pairs of activity metrics, estimated by kernel smoothing, for all data used in influence regression, as in **a** ( $n = 264,182$  pairs). Spearman correlation coefficients between pairs of metrics ( $c$ ) are overlaid on each plot. Signal correlation vs. distance,  $c = -0.021$ ,  $P = 4.8147 \times 10^{-264}$ ; noise correlation vs. distance,  $c = -0.067$ ,  $P = 7.7929 \times 10^{-28}$ ; noise correlation vs. signal correlation,  $c = 0.307$ ,  $P < 1 \times 10^{-100}$ . **c**, Left, piecewise linear distance predictors.  $25-150 \mu\text{m}$ , offset  $P < 1 \times 10^{-4}$ , slope  $P < 1 \times 10^{-4}$ ;  $150-450 \mu\text{m}$ , offset  $P < 1 \times 10^{-4}$ , slope  $P = 0.6598$ ;  $>450 \mu\text{m}$ , offset  $P = 0.0024$ , slope  $P = 0.089$ . Influence regression coefficient estimates and  $P$  values based on bootstrap. Grey line, median; box, 25–75% interval; whiskers, 1–99% interval. Right, activity predictors from the same model. Signal correlation,  $P = 0.0114$ ; signal  $\times$  distance,  $P = 0.4814$ ; noise correlation,  $P = 0.4622$ ; noise  $\times$  distance,  $P < 1 \times 10^{-4}$ ; signal  $\times$  noise,  $P = 0.7466$ ;  $n = 264,182$  pairs. **d**, Coefficient estimates from separate models, based on **c**, using the specified tuning component correlation instead of signal correlation, and pairs in which both neurons exhibited tuning for that feature. Direction,  $P = 0.9538$ ,  $n = 158,855$  pairs; orientation,  $P = 0.014$ ,  $n = 158,855$ ; spatial frequency,  $P = 0.83$ ,  $n = 202,941$ ; temporal frequency,  $P = 0.00026$ ,  $n = 59,228$ ; running speed,  $P = 0.1516$ ,  $n = 106,000$ . **e**, Coefficient estimates from separate models for components related to raw spike-triggered average receptive fields or features extracted from fitted Gabors.  $n = 113,794$  pairs for each feature. STA correlation,  $P = 0.0068$ ; Gabor correlation,  $P = 0.0047$ ; distance between Gabor centers,  $P = 0.00604$ ; ON overlap,  $P = 0.07548$ ; OFF overlap,  $P = 0.00004$ ; ON+OFF overlap,  $P = 0.0012$ ; single-field overlap,  $P = 0.2926$ . **f**, Influence versus signal correlation. Percentile bins, 15% half-width. Shading, mean  $\pm$  s.e.m. calculated by bootstrap. **g**, Influence versus noise correlation, for nearby (black,  $n = 49,942$ ) or distant (gray,  $n = 214,240$ ) pairs. Percentile bins, 20% half-width. Qualitatively similar results were obtained when varying distance thresholds by up to  $50 \mu\text{m}$  (not shown). **h**, Influence versus difference in preferred orientation. Value bins, 15° half-width. **i**, Influence versus STA correlation. Percentile bins, 15% half-width. **j**, Influence versus fitted Gabor correlation. Percentile bins, 15% half-width. **k**, Influence versus OFF overlap. Percentile bins, 15% half-width. **l**, Influence versus ON+OFF overlap. Percentile bins, 15% half-width.

Figure 3.7: (continued)





tion, as has been shown in experiments in L<sub>2/3</sub> of V<sub>I</sub> (Chettih and Harvey, 2019). Influence was significantly positively related to signal correlation and was either negative or zero at more negative correlation values (Figure 3.7c, right; Figure 3.7f), supporting the idea that excitatory neurons in L<sub>4</sub> show amplification when activity is similar. Furthermore, the interaction term for signal correlation and distance was near zero, such that the positive relationship between signal correlation and anatomical distance remains constant even at greater distances (Figure 3.7c, right) and suggesting that factors beyond RF overlap contribute to excitatory influence over these longer spatial scales. Thus, neurons preferentially recruited responses from other cells with similar activity profiles from across hundreds of microns in a given imaging field of view.

Although pairwise response correlations are useful in that they encompass information about shared activity, which could come from either features that we did not measure or visual tuning-related properties, they are unable to directly reveal what components may be contributing to similar responses between neurons. We therefore examined which tuning and RF features might contribute to the positive relationship between signal correlations and influence. To do so, in a separate regression model, we replaced the signal correlation term with the correlations between neuron pairs of their tuning curves for direction, orientation, spatial frequency, and temporal frequency. We also included the mouse's running speed as a predictor due to studies showing that locomotion modulates V<sub>I</sub> responses, although *a priori* we anticipated that visual tuning features would be more likely to contribute to influence given that they are generated and shaped in V<sub>I</sub>, whereas running-related activity may simply be reflective of external inputs. Of these tuning components, direction, spatial frequency, and running speed were unrelated to influence, although neurons were still tuned to these features (Figure 3.5c, d). This suggests that while these features are represented in the local population, transformations of this information content do not ap-

pear to occur within L<sub>4</sub>. However, orientation tuning and temporal frequency were positively related to influence (Figure 3.7d, h), reproducing the positive relationship between signal correlation and influence described above. Recurrence in L<sub>4</sub> may therefore selectively transform this subset of visual features.

We also sought to relate influence to RF features in the same manner. The raw STA correlation, Gabor correlation, OFF overlap, and ON+OFF overlap between pairs of neurons were significantly positively related to influence (Figure 3.7e, i-l). Influence was also close to zero or negative when RF correlations or overlap metrics were dissimilar or close to zero, suggesting that neurons with more similar RFs amplify each other's activity, while neurons with dissimilar RFs either have no influence or tend towards suppression. These results are consistent with the result that influence is more positive for higher signal correlations, as these RF metrics reflect a shared preference for portions of visual space between neurons.

We find that strong excitation between nearby neuron pairs, a positive relationship with noise correlations at shorter distances, and a positive relationship with signal correlations and specific visual tuning properties that persists over spatial scales all contribute to influence between neurons. Excitatory influence can therefore be attributed in part to neurons with certain shared visual tuning and RF characteristics, suggesting that recurrent local microcircuit computations within L<sub>4</sub> amplify responses via like-to-like functional connectivity along specific feature axes.

## 3.6 METHODS

### 3.6.1 VISUAL STIMULI

Visual stimuli were displayed on a gamma-corrected 27-inch IPS LCD gaming monitor (ASUS MG279Q). The monitor was positioned at an angle of  $30^\circ$  relative to the animal and such that the closest point to the mouse's right eye was  $\sim 24$  cm away, with visual field coverage  $\sim 103^\circ$  in width and  $\sim 71^\circ$  in height. Visual stimuli were generated using PsychoPy (Peirce, 2007) or Psychtoolbox. Prior to each experiment, using the retinotopic map from widefield imaging and a movable flashing square stimulus, the monitor was moved such that stimuli in the center of the monitor strongly drove neurons in the field of view imaged in that experiment. Seeding blocks to visualize orientation- and direction-tuned neurons and assist in manual selection of targets for photostimulation consisted of 100% contrast square-wave gratings with drift direction  $45^\circ$  apart presented for 3 seconds, followed by 3 seconds of gray. The visual stimuli in influence blocks consisted of square-wave drifting gratings at 10% contrast, direction from  $45^\circ$  to  $360^\circ$  in  $45^\circ$  increments, spatial frequency of 0.04 cycles per degree, and temporal frequency of 2 Hz (2 cycles per second). Stimuli were presented for 500 ms, followed by a 500 ms gray stimulus during the inter-stimulus interval (1 Hz presentation). The random gratings tuning measurement block used 80% contrast sine-wave gratings presented for 2 seconds with a 1 second gray inter-stimulus interval, with grating parameters sampled from the following uniform distributions:  $0$ - $360^\circ$  for direction,  $0.01$ - $0.16$  cycles per degree for spatial frequency, and  $0.5$ - $4$  Hz for temporal frequency. Both sets of gratings were presented on a gray background to match average luminance across stimuli and windowed gradually with a Gaussian aperture mask. The contrast-modulated Gaussian white noise (Niell and Stryker, 2008) tuning block consisted of movies with a 10 second

sinusoidally contrast-modulated period from gray to full-contrast to gray, with a random spatiotemporal spectrum in the Fourier domain,  $1/f$  power spectrum with spatial frequency maximum at 0.12 cycles per degree, and flat temporal frequency spectrum with a cutoff at 4 Hz. For influence blocks, the computer controlling the visual stimuli output digital triggers that initiated simultaneous photostimulation. For all blocks, digital triggers from the computer controlling visual stimuli were recorded simultaneously with the output of the ScanImage frame clock for offline alignment.

### 3.6.2 EXPERIMENTAL PROTOCOL

Before data acquisition, mice were habituated to handling, head-fixation on a spherical treadmill (Harvey et al., 2012), and visual stimuli for 2–4 days. For each experiment, a field of view (FOV) was selected based on expression levels of GCaMP and opsin. An average power of  $\sim 100$  mW (measured after the objective) was used for imaging in L4. For the water immersion lens, we used water that was boiled and then cooled, as we found that this prevented bubble formation over the long experiments and improved imaging stability. Multiple experiments conducted in each animal were performed at different locations within V1 or different depths within layer 4 (290–390  $\mu\text{m}$  below the brain surface, median 336  $\mu\text{m}$ ). Before each experiment, the monitor position was adjusted such that a movable flashing stimulus or drifting grating in the center of the screen drove the strongest responses in the imaged FOV, as determined by online observation of neural activity. Once a FOV was chosen, a baseline image from the resonant imaging path ( $\sim 575 \times 575$   $\mu\text{m}$ ) was stored and used throughout the entire experiment to compare with a live image of the current FOV and manually correct for axial and lateral drift (typically  $< 3$   $\mu\text{m}$  between blocks and  $< 10$   $\mu\text{m}$  over the full experiment) by adjusting the stage. A single experiment

consisted of a seeding block of  $\sim 5$  minutes, three influence blocks of 40–60 minutes each, a random gratings tuning block of 1 hour, and a contrast-modulated Gaussian white noise movie block of 35–40 minutes. Together with tuning maps for direction and orientation from seeding blocks, images from both the imaging and photostimulation pathway were used to visualize GCaMP and opsin expression and select regions of interest for photostimulation. Within each photostimulation block, each stimulation target was pseudo-randomly selected without replacement and activated at 1 Hz, such that all targets were activated in near-random order with an identical number of repeats (180 trials per site, typically 7,200–9,000 trials total per experiment). Drift and image quality stability of the experiment were verified post hoc by examining 1,000  $\times$  sped-up movies of the entire experiment after motion correction and temporal down-sampling, and experiments that were unstable were discarded without further analysis.

The full dataset consisted of 48 experiments from 3 male and 8 female mice, with 400 control sites and 1,398 neuron photostimulation sites, where 1,345 were significantly photostimulated (96.2%). In total, 13,950 neurons were recorded, resulting in 392,813 pairs of target and non-targeted neuron responses. Of the recorded neurons, 11,524 passed Gaussian process regression fit quality criteria (described below), Of all pairs, 4,196 pairs were excluded by a local 25  $\mu\text{m}$  distance threshold, and an additional 1,818 pairs were excluded by spatial overlap (described below). This left 264,182 pairs that passed all criteria for targeted and non-targeted neurons. Note that we refer to “non-targeted” neurons as those that were not directly targeted for photostimulation on that subset of trials, but a targeted neuron could become a non-targeted neuron on a different set of trials, and vice versa. Data from experiments were stored and analyzed using a custom-built pipeline within the DataJoint framework in MATLAB (Yatsenko et al., 2018).

### 3.6.3 SEEDING BLOCK-SPECIFIC PROCESSING

Images from seeding blocks were motion-corrected using a 2D cross correlation-based technique and then synchronized to visual stimulus frames. The circular variance, used as a measure of selectivity, was calculated from responses to each grating (7 different drift directions) in the orientation and direction domains and summed vectorially for each pixel in the field of view (Ringach et al., 2002). These vectors were displayed as a map where color corresponded to angle of the preferred orientation or direction of the resultant, and color intensity reflected the magnitude (i.e., selectivity for that angle) of the resulting vector (Bonhoeffer and Grinvald, 1993). The pixel maps were then used in combination with manual online examination of GCaMP and opsin expression to select neuron targets for photostimulation for each experimental session.

### 3.6.4 PHOTOSTIMULATION-SPECIFIC PRE-PROCESSING

We manually examined all sources identified near the location of each target photostimulation site, and when we did not observe an unambiguous match between a neuron source and intended target, we labeled that target as “unmatched” and excluded it from further analysis (195 photostimulation targets). For each matched photostimulation target, we calculated photostimulation-triggered average (PTA) fluorescence images for each experimental session’s FOV using 25 frames (~825 ms) before versus 27 frames (~890 ms) after photostimulation (e.g., Figure 2.3d). Because a photostimulated neuron’s processes could potentially overlap with other non-targeted cellular sources and contaminate the activity traces of those sources, we used a binarized version of the PTA to create a spatial footprint for the targeted neuron and excluded any target-nontarget pairs that overlapped. This primarily removed overlapping pairs that were <100  $\mu\text{m}$  apart.

### 3.6.5 NEURON RESPONSE MAGNITUDE TO PHOTOSTIMULATION AND RANDOM GRATINGS

Photostimulation response magnitude was calculated as the average  $\Delta F/F$  for 0-825 ms following photostimulation onset, minus  $\Delta F/F$  for 200 to 33 ms before photostimulation. For this analysis only, each neuron's  $\Delta F/F$  trace for the random gratings tuning block and Gaussian noise movie block was smoothed to reduce the impact of imaging noise using a Savitzky-Golay filter of polynomial order 5 and a frame length of 2 seconds. The magnitude of responses to optimal visual stimuli during the random gratings block and Gaussian noise movies block was then calculated as the 95th percentile of the distribution of the difference between the 99th and 1st percentiles of each trace over all trials (3 seconds and 10 seconds each, respectively).

### 3.6.6 INFLUENCE CALCULATIONS

To quantify influence, we used a  $\Delta$ Activity metric as previously described (Chettih and Harvey, 2019). For each neuron, single-trial responses were calculated as the average value of deconvolved activity over 31 imaging frames (1 second) from photostimulation onset. For a given neuron  $n$  on photostimulation trial  $i$ ,  $\Delta$ Activity $_{i,n}$ , or single-trial residual, was calculated as the difference between the activity on that trial and the average activity on control site photostimulation trials  $j$  in which the low-contrast grating stimulus was the same as on trial  $i$ , excluding trials where the stimulated neuron was within 25  $\mu$ m. This corresponds to:

$$\Delta\text{Activity}_{i,n} = \text{Activity}_{i,n} - \left\langle \text{Activity}_{j,n} \right\rangle_j$$

This single-trial influence value was then normalized by dividing by the neuron’s standard deviation over all trials  $i$  in order to standardize relative to the variability in activity for each neuron. For an individual photostimulation target site, influence was calculated as the average  $\Delta\text{Activity}_{i,n}$  over all trials  $i$  in which the target was photostimulated. For analysis of control site influence, for each control site in an experiment, we used a leave-one-out procedure in which one control site was excluded from trials  $j$  used in the calculation described above.

To determine whether a target was significantly photostimulated, we used a parametric shuffle estimate in which we computed 100,000 random permutations of trial number and photostimulation target (excluding trials with target photostimulation within 25  $\mu\text{m}$  of a neuron), and compared those to average photostimulation responses to individual targets over all trials. A threshold of 5 standard deviations above shuffle was used for significance, and only photostimulation of neuron sites where the average response was 5 standard deviations greater than expected in the shuffled distribution were used in influence-related analyses.

### 3.6.7 GAUSSIAN PROCESS REGRESSION AND TUNING

We used a random gratings tuning measurement block, where the parameters for the visual stimulus presented on each trial were randomly sampled over a wide range of values for each feature (drift direction, spatial frequency, and temporal frequency). Although this allowed us to cover a broader range of stimulus parameters as compared to conventional experiments in which a set of stimuli are repeated many times, because no two stimuli were identical, there were no repeats of a stimulus over the course of a session and we thus could not average responses over repeats. As a result, we turned to Gaussian process (GP) regression as a method to interpolate neural responses between highly similar, but not identical trials (Chettih and Harvey, 2019). GP regression is a



nonparametric Bayesian modeling approach that aims to find a probability distribution or function that models similarities between data points in a high-dimensional space. We therefore fit GP regression models to the data, which consisted of four dimensions: gratings drift direction, gratings spatial frequency, gratings, temporal frequency, and the mouse’s running speed. Single-trial responses for each neuron, which were computed as the average of deconvolved activity over 61 frames of visual stimulus presentation ( $\sim 2$  seconds), after which a square-root transform was performed to approximately stabilize the noise variance (Yu et al., 2009), were considered as noisy observations of a 4D latent function that specifies the tuning of a neuron, which the GP model predicts. Models were built using the GPML MATLAB toolbox, version 4.2 (Rasmussen and Williams, 2006).

The GP model is specified by a covariance function and its hyperparameters, which specifies the distance or similarity of function values between data points in the 4D tuning space. We used a squared exponential covariance kernel function  $k(x, x')$ , one of the most widely used, as it is used to model smooth functions. All hyperparameters were selected by optimizing the marginal likelihood. The hyperparameters include the scale of the covariance function  $\sigma_c^2$ , as well as individual length scales that are defined for each input tuning dimension (note that drift direction was first projected into the complex plane) in diagonal matrix  $P$  with entries  $\lambda_1^2, \dots, \lambda_4^2$ , for which larger values mean that the function is smoother and shows less sharp tuning. This is formalized as:

$$k(x, x') = \sigma_c^2 \exp(-(x - x')P^{-1}(x - x'))$$

We used a Gaussian likelihood function with a hyperparameter for the level of response variability, such that finite samples of the latent function and noisy observations at arbitrary locations

have joint Gaussian distributions. By conditioning the joint Gaussian distribution on the observations (the training set), we can then sample from the joint posterior distribution to generate values at unobserved locations (the test set).

As a metric for model accuracy, we divided each neuron's responses in the gratings block ( $\sim 1,200$  trials) into 20 subsets and predicted responses for each subset ("test") using data from the other 19 subsets ("train"), and then correlated the predictions with actual recorded data. We compared model train and test accuracy to visualize overfitting (Figure 3.5b) and draw a threshold for which neurons to consider for GP tuning-based analyses. Signal correlations were computed as the Pearson's linear correlation coefficient between GP model single-trial test predictions on held-out data (using 20-fold cross-validation for predictions on all trials) for each pair of neurons. We considered these to be equivalent to the standard definition for signal correlations computed on mean responses to a discrete set of stimuli, as the GP predictions are average responses inferred from interpolation between trials of similar stimulus parameters. Noise correlations were computed as the Pearson's linear correlation of single-trial residuals, calculated from model predictions on test data and actual single-trial responses, using the same procedure on held-out data described above. Using the same reasoning as for signal correlations, this definition for noise correlations is also equivalent to the typical definition. Because signal and noise correlations were based on GP model fits, we removed neurons with poorly-fit models from subsequent analyses by setting the following inclusion criteria: each neuron in a photostimulation target-nontarget pair needed to have model accuracies (Pearson correlation between predicted and actual responses) of  $>0.2$  and a difference between train and test accuracies of  $<0.15$  to exclude overfit neurons, as described above. Note that these inclusion criteria applied only to analyses in which tuning was considered (i.e., not to analyses of influence and distance, neuron versus control site influence,

etc.).

Because the GP model fits to neural responses were in the form of a nonlinear 4D tuning function, we extracted 1D tuning curves by examining a dimension while fixing the other dimensions at the values that each showed the highest response, and repeating this for all dimensions. For example, we fixed spatial frequency, temporal frequency, and the mouse's running speed at the values that drove the highest amount of neural activity, and then looked at drift direction tuning. To do so, we found the location where the latent response was maximized by starting at the location of the maximal single-trial prediction, and then using a grid search over nearby locations in 4D. Once this location was determined, we then fixed three dimensions and varied the fourth, as described above, to extract a tuning curve. Preferred stimulus values were also extracted from these tuning curves. The tuning curves were also used to determine how strongly each neuron was tuned to each tuning dimension by calculating a depth of modulation index  $DOM_d$  for each dimension  $d$ , which was defined as follows:

$$DOM_d = \frac{\max(t_d) - \min(t_d)}{\sqrt{\sigma_{\max(t_d)}^2 + \sigma_{\min(t_d)}^2}}$$

where  $t_d$  is the tuning curve for a neuron for the  $d^{th}$  dimension, and  $\sigma_{\max(t_d)}^2$  and  $\sigma_{\min(t_d)}^2$  are the variance of the posterior distribution at the maximum and minimum tuning value locations, respectively. Neurons with a  $DOM > 2$  for a given dimension were considered significantly tuned. When tuning for individual features was considered in an analysis, only neurons passing this significance threshold were used (Figure 3.5, Table 3.1).

Tuning dimension	Number of neurons	% of tuned neurons	% of all neurons
Drift direction	8,099	78	64
Spatial frequency	10,175	88	73
Temporal frequency	5,701	49	41
Running speed	7,254	63	52

**Table 3.1: Significantly tuned neurons for each tuning dimension, from GP regression.** Number of neurons: neurons passing GP fit criteria and  $DOM > 2$ ; percentage of tuned neurons, denominator is total number of neurons passing GP fit criteria; percentage of all neurons, denominator is total number of recorded neurons.

### 3.6.8 GAUSSIAN NOISE MOVIES

In addition to the influence and gratings tuning blocks described above, we also included an experimental block in which we displayed contrast-modulated Gaussian noise movies (Niell and Stryker, 2008) for  $\sim 40$  minutes to estimate linear receptive fields (RFs). The movies were generated with a random spatiotemporal frequency spectrum in the Fourier domain. Spatial frequency dropped off as  $A(f) \sim 1/(f + f_c)$ , where  $f_c = 0.05$  cycles per degree (cpd) and with a maximum spatial frequency of  $0.12$  cpd. The temporal frequency spectrum was flat with a sharp cutoff at  $4$  Hz. The spectrum was inverted to generate a spatiotemporal movie at  $2560 \times 1440$  pixels and displayed at  $60$  frames per second. Each movie was  $10$  seconds long and cycled sinusoidally from  $0\%$  to  $100\%$  contrast and back to  $0\%$  contrast. A total of  $\sim 240$  movies were played, for  $\sim 40$  minutes of total presentation.

### 3.6.9 RECEPTIVE FIELD MEASUREMENT

Linear RFs were estimated from the Gaussian noise movie tuning block. The movie resolution was downsampled by a factor of  $3$  for computational efficiency and the movies were shifted by  $3$  frames ( $\sim 100$  ms) to account for lag (e.g., from the delay between visual stimulus generation and display on the monitor, latency in spikes from the retina to the brain, GCaMP fluorescence).

The spike-triggered average (STA) images, or linear RFs, of the contrast-modulated noise movie responses was calculated as the reverse correlation of deconvolved neuronal activity with the images. To determine whether the RF for a given neuron was significant, we adapted a previously described procedure (Cossell et al., 2015). For each neuron, we randomly shuffled the response vector of spiking activity to the movie sequence and repeated the reverse correlation. This procedure was repeated 100 times to produce 100 shuffled RFs, from which the mean ( $\mu_{\text{shuffle}}$ ) and standard deviation ( $\sigma_{\text{shuffle}}$ ) were calculated. RFs that contained any pixels with absolute values  $> \mu_{\text{shuffle}} + 5 * \sigma_{\text{shuffle}}$ , where 5 denotes the number of standard deviations from the mean, were defined as significant. Using this definition, the fraction of neurons with significant RFs was 42.7% (5,954/13,950, range over sessions: 22.2%–65.2%).

We parameterized RFs by fitting a two-dimensional elliptical Gaussian function, hereafter referred to as Gabor. The general function is described by

$$G(x, y) = A_0 + A \exp[-(a(x - x_0)^2 + 2b(x - x_0)(y - y_0) + c(y - y_0)^2)]$$

where

$$a = \frac{\cos^2 \theta}{2\sigma_X^2} + \frac{\sin^2 \theta}{2\sigma_Y^2}$$

$$b = \frac{\sin 2\theta}{4\sigma_X^2} + \frac{\sin 2\theta}{4\sigma_Y^2}$$

$$c = \frac{\sin^2 \theta}{2\sigma_X^2} + \frac{\cos^2 \theta}{2\sigma_Y^2}$$

and  $A_0$  is a constant term,  $A$  is the amplitude,  $(x_0, y_0)$  is the center of the Gaussian,  $\sigma_X$  and  $\sigma_Y$  are standard deviations of the Gaussian perpendicular and parallel to the grating axis, and  $\theta$  is orientation.

To ensure that only Gabors that were well-fitted to the raw STAs were used for analysis, we imposed an additional criterion that the pixel–pixel Pearson’s correlation coefficient between a neuron’s raw STA and fitted Gabor needed to be  $>0.3$ . Under this requirement, 29.3% of neurons ( $n = 4,086$ ) both were significant and passed this fit quality control measure. The Gabor fits were also used to define ON and OFF subregions (Figure 3.6). ON subfields were defined as regions of the fitted Gabor with pixels that were  $>20\%$  of the maximum absolute value of the Gabor, and OFF subfields were defined as regions of the fitted Gabor with pixels that were  $<20\%$  of the negative of the maximum absolute value of the Gabor (Cossell et al., 2015). The amount of overlap ( $0 \leq \text{overlap} \leq 1$ ) between a target-nontarget neuron pair was defined as

$$\frac{|A \cap B|}{|A \cup B|}$$

or

$$\text{Overlap}_{\text{ON+OFF}} = \frac{|(A_{\text{ON}} \cap B_{\text{ON}}) + (A_{\text{OFF}} \cap B_{\text{OFF}})|}{|(A_{\text{ON}} \cup B_{\text{ON}}) + (A_{\text{OFF}} \cup B_{\text{OFF}})|}$$

where  $A$  and  $B$  are the regions of visual space covered by a target and non-targeted neuron’s ON, OFF, or both (ON+OFF) subfields. We also developed an overlap metric that we called “single-field overlap,” in which we combined the ON and OFF subfields into one subfield and computed overlap in the same way as described above. For RF-associated analyses, a total of 113,794 pairs (113,794/386,799 = 29.4%) of target-nontarget RFs (where targeted neurons were significantly photostimulated, showed no overlap with non-target neuron sources, were at least 25  $\mu\text{m}$  away, each neuron’s raw STA RF was significant, and the fitted Gabor had a correlation coefficient of  $>0.3$  with the raw STA) were used. When adding in an additional requirement that these neurons needed to also pass GP fit quality criteria as described above, 83,997 pairs (21.7%) were used in

analysis.

### 3.6.10 INFLUENCE REGRESSION AND ASSOCIATED ANALYSES

We used two approaches to analyze influence values. First, we used multiple linear regression (Figure 3.7c-e) to understand the relationship between activity metrics (anatomical distance with signal or noise correlations) and influence. The columns of the design matrix included piecewise linear terms for distance ( $<150\ \mu\text{m}$ ,  $150\text{--}450\ \mu\text{m}$ , and  $>450\ \mu\text{m}$  segments), linear terms for signal correlation and noise correlation and an interaction term between them, and linear interaction terms between signal correlation and noise correlation with log-transformed distance. Predictors were  $z$ -scored so that coefficient magnitudes could be fairly compared. We estimated regression coefficients for each predictor from 10,000 data points that were resampled for each. From these bootstrapped distributions, we obtained median coefficients, confidence intervals, and  $P$  values (described below). For tuning and RF components regression, we constructed separate alternate regression models in which signal correlation and interactions were replaced by tuning curve correlations or RF features. For each of these features, data were restricted to neuron pairs that passed photostimulation and tuning criteria (i.e.,  $>25\ \mu\text{m}$  apart, no spatial footprint overlap, GP fit quality criteria described above, or RF fit quality criteria described above). Note that the GP regression model predicted grating drift direction over  $360^\circ$ , so we extracted direction tuning curves by computing the difference across both directions ( $0\text{--}180^\circ$  and  $181\text{--}360^\circ$ ) over each orientation, and extracted orientation tuning curves by averaging tuning curves across both directions for each orientation.

We also computed running averages for influence versus different metrics (Figure 3.7f-l). We chose center locations to span the full range of values for the metric, and manually specified

bin width in either percentile space or real value space. In each plot,  $x$  values were the average value of the smoothed variable within a bin, and standard error for each bin was estimated using bootstrapping. The 1D average plots were used as a complementary visualization to the multiple linear regression analyses.

### 3.6.11 STATISTICS

The statistical tests used were generally non-parametric. To calculate standard errors, we recalculated a test statistic (e.g., mean or standard deviation) on 1,000 samples from the full dataset with replacement, and then took the standard deviation over bootstraps. To determine significance of coefficients from influence regression, we repeated the influence regression calculation 10,000 times on resampled data. Plots showing regression coefficients (Figure 3.7c-e) are shown as the percentiles of this bootstrap distribution.  $P$  values reported are calculated as two times the fraction of the distribution where the coefficient was 0 or opposite sign of the median value.



# 4

## Discussion and Future Experiments

### 4.1 FEATURE-SPECIFIC AMPLIFICATION WITHIN $V_I$ L<sub>4</sub>

#### 4.1.1 SUMMARY

By manipulating activity in neurons with identified tuning properties, we have explored the local transformations that L<sub>4</sub> of  $V_I$ , the main input layer from thalamus, performs during visual processing. We first developed an approach to co-express an opsin and a calcium indicator in excitatory L<sub>4</sub> neurons. During visual stimulus presentation to awake mice, we used two-photon

optogenetic stimulation of individual cells while imaging responses of the local population. Separately, we characterized the activity and tuning profiles of L4 neurons to different sets of visual stimuli in order to build an understanding of how functional properties relate to neuron-neuron influence. Using the influence mapping technique, we have shown that L4 contains signatures of feature-specific amplification.

Multiple components contributed to influence in L4. First, excitatory neurons showed strong local influence, which decayed over greater anatomical distances between neuron pairs. This effect could be related to amplification based on greater similarity in representations of visual field position. Second, influence was also positively related to noise correlations at short but not long intersomatic distances, pointing towards a role of local connectivity in driving shared variability in nearby neurons, in combination with common feedforward inputs that also affect broader spatial scales. Third, signal correlations also had a positive relationship with influence, but in a distant-invariant manner, such that neurons with similar activity profiles tended to recruit activity from one another regardless of their distance apart. Not all tuning properties examined were related to amplification. This is perhaps unsurprising, as having highly constrained excitatory connectivity over many features would lead to very little action potential generation and would likely be an unusable circuit architecture. We found that amplification was specific to neurons with certain preferred visual stimulus features and shared RF properties. The specificity in amplification for features such as orientation, temporal frequency, and RF overlap provides support for the idea that these representations are locally transformed within L4, unlike others that are instead reflective of inputs to L4. Together, these factors that contribute to influence provide new causal evidence for the existence of a like-excites-like computation in L4.

#### 4.1.2 COMPARISON TO PREVIOUS RESULTS

Anatomy-informed computational modeling studies have proposed that recurrent intracortical excitation in L4 amplifies incoming thalamic signals (Douglas et al., 1995; Somers et al., 1995; Van Vreeswijk and Sompolinsky, 1996). Previous experimental studies have supported this idea and shown that L4 in V1 amplifies the magnitude of incoming weak thalamic sensory responses without altering their tuning (Li et al., 2013b; Lien and Scanziani, 2013). Similar observations of intracortical excitation of thalamocortical inputs have also been made in L4 of auditory cortex (Li et al., 2013a). In addition, visual RFs in L4 were shown to be smaller but with the same shape when cortical activity was silenced, suggesting that expansion of RFs occurs from horizontal intracortical excitatory circuitry recruiting additional inputs with a bias along the L4 cell's preferred orientation (Li et al., 2013b). However, the exact mechanism by which these phenomena occur has not been shown. A recent study with biophysically-detailed modeling has proposed that like-to-like functional connectivity is necessary in L4 to reach physiological levels of tuning selectivity (Arkhipov et al., 2018). Prior to our work with influence mapping in L4, how this amplification can occur had not been directly tested or shown experimentally. Our result that L4 performs feature-specific amplification is consistent with these studies and, to our knowledge, provides the first direct causal evidence that this computation arises via like-to-like functional connectivity.

#### 4.1.3 FUNCTION OF AMPLIFICATION

Amplification within L4 could increase the gain of responses to sensory stimuli, such that the signal of stimulus-relevant information is boosted and has higher fidelity before then being relayed to downstream targets. This type of computation in L4 could also be important for performing

pattern completion from noisy or degraded sparse inputs to expand and stabilize the representation of visual information content. Once this reliable neural code is established within the cortex in L<sub>4</sub>, downstream recipient neurons in L<sub>2/3</sub> could then use these more robust inputs to do inference of the underlying visual stimulus properties. This process could be further aided by local L<sub>2/3</sub> circuitry employing feature competition to suppress redundant information and create a more efficient neural code, as has been proposed by previous work (Chettih and Harvey, 2019; Olshausen and Field, 1997, 2004).

#### 4.2 UTILITY OF INFLUENCE MAPPING

Influence mapping is not a replacement for approaches that measure anatomical connectivity such as structural microscopy or physiology, but serves as a complementary technique that builds upon this type of work and provides functional, causal measurements of microcircuit architecture *in vivo* that may not have been intuitive otherwise. For example, a neural network with a particular connectivity structure might operate in fundamentally different regimes depending on factors such as the visual inputs it receives or more general modulatory processes like attention and arousal. Predicting computations *in vivo* may therefore not be directly possible from connectivity measurements alone, demonstrating a need for methods that use manipulations to study functional interactions between neurons. One *in silico* demonstration of this comes from a recent study that used simulated optogenetic perturbations in a model of V<sub>1</sub> constrained by experimental data (Cai et al., 2020). In general, there were transitions between like-to-like excitation and inhibition (i.e., robustness versus redundancy reduction) depending on visual stimulus contrast. These results demonstrate that within recurrently-connected networks with fixed connectivity, perturbation-based techniques can reveal computations that differ based on network

state, highlighting the need for these types of causal methods to understand functional neural architectures.

### 4.3 MODIFICATIONS AND ADDITIONAL EXPERIMENTAL DIRECTIONS

There are a number of possible modifications to the influence mapping experiments that have been described in the previous chapters. As would be predicted from computational studies, it is also plausible that depending on the types of perturbations used (e.g., multi-neuron photostimulation), visual stimuli and their parameters (e.g., high contrast stimuli, natural images), or behavioral context (e.g., visual detection or discrimination tasks), different types of computations may be revealed. This work acts as a foundation for future studies to further characterize the functional structure of  $V_I$ .

#### 4.3.1 INFLUENCE AT THE POPULATION VERSUS SINGLE-NEURON LEVEL

Because influence measurements from individual neuron pairs were noisy in our experiments, we chose to focus on analyses at a population level by pooling data over the thousands of pairs recorded in each experimental session. Subsequent experiments could instead focus on photostimulating fewer targets but increasing the total number of stimulation trials per target, in order to build up statistical significance on a single-pair basis rather than relying on averaging over large populations. This approach would then allow for claims about the influence of individual neurons.

#### 4.3.2 DECREASING OPSIN DENSITY TO IMPROVE PHOTOSTIMULATION RESOLUTION

We used fairly dense expression of opsin in L4 neurons. To improve resolution and further reduce effects from off-target photostimulation, an alternative expression strategy is to still express Cre-dependent GCaMP in *Scnn1a-Tg3-Cre* mice, but use Cre-dependent Flp with Flp-dependent opsin. GCaMP expression would continue to be dense, but the sparseness of opsin expression could be tuned independently from GCaMP, which was not possible with the labeling approach used in the experiments described in previous chapters.

#### 4.3.3 ALTERNATIVE VISUAL STIMULI

During influence blocks, mice passively viewed low-contrast drifting gratings. Computations within V1 may depend on the intensity of visual stimulation (i.e., low or high contrast), which could recruit different relative levels of excitation and inhibition for visual detection versus discrimination modes (Polat et al., 1998). Under conditions of increasing visual stimulus contrast, computations may shift from amplification, which may be beneficial for detection, to competition in order to suppress runaway excitation and sharpen tuning for discrimination. It therefore would be of importance to conduct experiments under different stimulus contrasts to probe these types of questions. In addition, although drifting gratings have commonly been used to study V1, they are a simplistic stimulus and are not fully representative of scenes that an animal might encounter in its lifetime. To understand influence during presentation of a more ethologically relevant visual stimulus, an alternative could be to show natural movies (David et al., 2004; de Vries et al., 2020; Yoshida and Ohki, 2020) during photostimulation.

#### 4.3.4 INHIBITION IN L<sub>4</sub>

We did not examine the role of inhibition within L<sub>4</sub>. However, to build up a more complete picture of the functional architecture of L<sub>4</sub>, it will be important to understand whether inhibitory neurons act as gain control or response normalization of excitatory activity (Hofer et al., 2011; Kerlin et al., 2010; Packer and Yuste, 2011), although this seems unlikely given the specificity of influence, or instead interact with excitatory neurons in a more structured manner (Runyan et al., 2010; Wilson et al., 2012; Yoshimura and Callaway, 2005; Znamenskiy et al., 2018). Possibilities for future experiments include photostimulating L<sub>4</sub> excitatory neurons while imaging responses in both excitatory and inhibitory neurons, including a nuclear label for the latter (e.g., with the mDlx enhancer) to differentiate between cell types online; another variant is to instead stimulate inhibitory neurons to understand their influence on the local network with respect to tuning. Because previous studies have proposed different roles for inhibitory neuron subtypes such as parvalbumin, somatostatin, and vasoactive intestinal peptide-expressing interneurons (Adesnik et al., 2012; Chen et al., 2015; Dipoppa et al., 2018; El-Boustani and Sur, 2014; Fu et al., 2014; Khan et al., 2018; Kvitsiani et al., 2013; Ma et al., 2010; Makino and Komiyama, 2015; Pakan et al., 2016; Pfeffer et al., 2013; Pi et al., 2013; Poort et al., 2015; Wilson et al., 2012; Xu et al., 2013; Yang et al., 2016), these experiments could be combined with post-hoc immunostaining, transgenic mouse lines with inhibitory neuron-specific Cre expression, or viruses with subtype-specific enhancer elements. Interneuron subtypes may show distinct structures of influence, which could support unique roles in contributing to cortical computations. For example, representations could be sharpened with tuned inhibition in like-inhibits-unlike motifs. Another possibility is that inhibition could influence excitatory inputs to generate new properties, such as direction selectivity. By combining excitatory and inhibitory influence mapping analyses, it may

be possible to understand how the interplay of cell type-specific influence contributes to cortical computations in L<sub>4</sub>.

#### 4.3.5 TRANSFORMATIONS BETWEEN CORTICAL LAYERS

Understanding how information is transformed between cortical layers is an open area of research. One classical proposed transformation comes from influential early studies from Hubel and Wiesel, in which the generation of complex cells in superficial layers was proposed to arise from integration of feedforward simple cell inputs from deeper layers (Hubel and Wiesel, 1962). Work in anesthetized cats demonstrated that inactivating L<sub>4</sub> suppressed L<sub>2/3</sub> complex cell activity (Martinez and Alonso, 2001). In mouse V<sub>1</sub>, the distribution of simple and complex cells across layers is skewed such that complex cells are more numerous in L<sub>2/3</sub> than in L<sub>4</sub> (Li et al., 2015), consistent with the model in which complex cells are synthesized from summation of convergent simple cell inputs. Photostimulating ON/OFF phase-offset iso-oriented L<sub>4</sub> simple cells, which would be predicted to activate neurons with phase-invariant complex activity in L<sub>2/3</sub>, would directly test these long-standing hypotheses about the mechanism of complex cell RF formation. Another test could be to stimulate L<sub>4</sub> cells with spatially offset RFs, which might recruit L<sub>2/3</sub> neurons with elongated receptive fields. Using influence mapping experiments, we can build upon existing literature using causal, functionally-defined manipulations to understand at a single-neuron level how higher-order representations are constructed in the visual system.

Another related line of exploration is understanding more generally how L<sub>4</sub> neurons influence each other versus how they influence L<sub>2/3</sub> neurons, which are proposed to be the primary recipients of feedforward excitation from L<sub>4</sub>. Are there similar like-to-like motifs between L<sub>2/3</sub> and



L4 as we have observed in local L4 experiments, and are there signatures of how selectivity for different tuning features might arise across layers? Connected L2/3 neurons have been shown to share common excitatory input from L4, which could explain inheritance of visual selectivity across layers (Yoshimura and Callaway, 2005; Yoshimura et al., 2005). Recent studies using transsynaptic retrograde tracing with two-photon imaging in mouse V1 found that presynaptic L4 networks exhibit similar orientation and direction tuning, which can match the preference of a starter postsynaptic L2/3 cell (Rossi et al., 2020; Wertz et al., 2015). Furthermore, L2/3 neurons are proposed to inherit orientation tuning from L4 inputs with similar preferred orientation that are arranged along the same axis in retinotopic space (Rossi et al., 2020). In a study of mouse L2/3 V1 combining *in vivo* calcium imaging with *in vitro* whole-cell recordings, ON+OFF overlap, OFF overlap, and RF correlation (in addition to response correlation) were found to best predict connection amplitude between pairs of neurons (Cossell et al., 2015) – the same features that we found to be positively related to influence in L4. One possibility is that L4 neurons recurrently amplify activity from other local neurons sharing those features, and this transformation is then inherited by L2/3. Together, these data suggest that fine-scale cortical subnetworks that are co-tuned for particular visual features combine to mediate processing of visual information and give rise to feature selectivity. Influence mapping could be applied to functionally-defined subsets of neurons to validate these models of how information is reshaped between cortical layers. To understand whether interlaminar computations are facilitated by inputs with similar functional properties and specific anatomical organization, it would be possible to photostimulate L4 neurons with defined functional properties while simultaneously imaging responses in L2/3.

#### 4.3.6 OTHER EXTENSIONS

Here, we have primarily discussed experiments to understand transformations within the primary input layer in  $V_1$ ,  $L_4$ , and its main targets in  $L_{2/3}$ . Future work could also examine the computations in cells labeled depending on their projection patterns or in downstream output layers 5 and 6 that project to other areas in the brain, which could therefore contain unique organizational motifs. Along a similar vein, it may also be interesting to perform influence mapping on different transcriptomic cell types. More generally, influence mapping could be used to probe computations in neural populations throughout processes that evolve over time, such as during development or learning.

#### 4.4 CONCLUSION

In Chapter 2 and 3, we have demonstrated the application of influence mapping in combination with characterizing visual tuning to understanding local computations within  $L_4$  of  $V_1$ , and we show that  $L_4$  performs feature-specific amplification. Previous techniques have lacked the ability to link synaptic and functional levels. Understanding how low-level features contribute to computations is also still relatively unknown, with many modeling studies frequently omitting these to limit complexity, which further motivates studying recurrent cortical networks without directly taking connectivity into account. The influence mapping approach is therefore a much-needed accompaniment to existing technologies and theoretical studies for understanding neural computations, and can be extended to many different lines of investigation.

# References

- Adesnik, H. & Scanziani, M. Lateral competition for cortical space by layer-specific horizontal circuits. *Nature* **464**, 1155–1160 (2010).
- Adesnik, H., Bruns, W., Taniguchi, H., Huang, Z. J. & Scanziani, M. A neural circuit for spatial summation in visual cortex. *Nature* **490**, 226–230 (2012).
- Andrasfalvy, B. K., Zemelman, B. V., Tang, J. & Vaziri, A. Two-photon single-cell optogenetic control of neuronal activity by sculpted light. *Proceedings of the National Academy of Sciences* **107**, 11981–11986 (2010).
- Arkhipov, A. *et al.* Visual physiology of the layer 4 cortical circuit in silico. *PLOS Computational Biology* **14**, e1006535 (2018).
- Averbeck, B. B. & Lee, D. Neural noise and movement-related codes in the macaque supplementary motor area. *Journal of Neuroscience* **23**, 7630–7641 (2003).
- Ayaz, A., Saleem, A. B., Schölvinck, M. L. & Carandini, M. Locomotion controls spatial integration in mouse visual cortex. *Current Biology* **23**, 890–894 (2013).
- Baker, C. A., Elyada, Y. M., Parra, A. & Bolton, M. M. L. Cellular resolution circuit mapping with temporal-focused excitation of soma-targeted channelrhodopsin. *eLife* **5**, 1–15 (2016).
- Barbour, D. L. & Callaway, E. M. Excitatory Local Connections of Superficial Neurons in Rat Auditory Cortex. *Journal of Neuroscience* **28**, 11174–11185 (2008).
- Bartolo, R., Saunders, R. C., Mitz, A. R. & Averbeck, B. B. Information-limiting correlations in large neural populations. *Journal of Neuroscience* **40**, 1668–1678 (2020).
- Bègue, A. *et al.* Two-photon excitation in scattering media by spatiotemporally shaped beams and their application in optogenetic stimulation. *Biomedical Optics Express* **4**, 2869 (2013).
- Benshalom, G. & White, E. L. Quantification of thalamocortical synapses with spiny stellate neurons in layer IV of mouse somatosensory cortex. *Journal of Comparative Neurology* **253**, 303–314 (1986).
- Billeh, Y. N. *et al.* Systematic Integration of Structural and Functional Data into Multi-scale Models of Mouse Primary Visual Cortex. *Neuron* **106**, 388–403 (2020).
- Binzegger, T. A Quantitative Map of the Circuit of Cat Primary Visual Cortex. *Journal of Neuroscience* **24**, 8441–8453 (2004).

- Bonhoeffer, T. & Grinvald, A. The layout of iso-orientation domains in area 18 of cat visual cortex: Optical imaging reveals a pinwheel-like organization. *Journal of Neuroscience* **13**, 4157–4180 (1993).
- Bonin, V., Histed, M. H., Yurgenson, S. & Reid, R. C. Local Diversity and Fine-Scale Organization of Receptive Fields in Mouse Visual Cortex. *Journal of Neuroscience* **31**, 18506–18521 (2011).
- Bopp, R., Holler-Rickauer, S., Martin, K. A. & Schuhknecht, G. F. An Ultrastructural Study of the Thalamic Input to Layer 4 of Primary Motor and Primary Somatosensory Cortex in the Mouse. *The Journal of Neuroscience* **37**, 2435–2448 (2017).
- Brecht, M., Roth, A. & Sakmann, B. Dynamic receptive fields of reconstructed pyramidal cells in layers 3 and 2 of rat somatosensory barrel cortex. *Journal of Physiology* **553**, 243–265 (2003).
- Cai, B. *et al.* Modeling robust and efficient coding in the mouse primary visual cortex using computational perturbations. *bioRxiv* (2020).
- Chaigneau, E. *et al.* Two-Photon Holographic Stimulation of ReaChR. *Frontiers in Cellular Neuroscience* **10**, 293–296 (2016).
- Chen, S. X., Kim, A. N., Peters, A. J. & Komiyama, T. Subtype-specific plasticity of inhibitory circuits in motor cortex during motor learning. *Nature Neuroscience* **18**, 1109–1115 (2015).
- Chettih, S. N. & Harvey, C. D. Single-neuron perturbations reveal feature-specific competition in V1. *Nature* **567**, 334–340 (2019).
- Chichilnisky, E. J. A simple white noise analysis of neuronal light responses. *Network: Computation in Neural Systems* **12**, 199–213 (2001).
- Chisum, H. J., Mooser, F. & Fitzpatrick, D. Emergent Properties of Layer 2/3 Neurons Reflect the Collinear Arrangement of Horizontal Connections in Tree Shrew Visual Cortex. *J. Neurosci.* **23**, 2947–2960 (2003).
- Coogan, T. A. & Burkhalter, A. Hierarchical organization of areas in rat visual cortex. *J. Neurosci.* **13**, 3749–72 (1993).
- Cossell, L. *et al.* Functional organization of excitatory synaptic strength in primary visual cortex. *Nature* **518**, 399–403 (2015).
- da Costa, N. M. & Martin, K. A. C. Selective Targeting of the Dendrites of Corticothalamic Cells by Thalamic Afferents in Area 17 of the Cat. *Journal of Neuroscience* **29**, 13919–13928 (2009).
- Daie, K., Svoboda, K. & Druckmann, S. Targeted photostimulation uncovers circuit motifs supporting short-term memory. *Nature Neuroscience* **24**, 259–265 (2021).
- dal Maschio, M., Donovan, J. C., Helmbrecht, T. O. & Baier, H. Linking Neurons to Network Function and Behavior by Two-Photon Holographic Optogenetics and Volumetric Imaging. *Neuron* **94**, 774–789 (2017).

- Dalgleish, H. W. *et al.* How many neurons are sufficient for perception of cortical activity? *eLife* **9**, 1–99 (2020).
- Dana, H. *et al.* High-performance calcium sensors for imaging activity in neuronal populations and microcompartments. *Nature Methods* **16**, 649–657 (2019).
- David, S. V., Vinje, W. E. & Gallant, J. L. Natural Stimulus Statistics Alter the Receptive Field Structure of V1 Neurons. *Journal of Neuroscience* **24**, 6991–7006 (2004).
- Dipoppa, M. *et al.* Vision and Locomotion Shape the Interactions between Neuron Types in Mouse Visual Cortex. *Neuron* **98**, 602–615 (2018).
- Douglas, R. J., Koch, C., Mahowald, M., Martin, K. A. C. & Suarez, H. H. Recurrent Excitation in Neocortical Circuits. *Science* **269**, 981–985 (1995).
- Douglas, R. J. & Martin, K. A. C. Neuronal Circuits of the Neocortex. *Annu. Rev. Neurosci* **27** (2004).
- Driscoll, L. N., Pettit, N. L., Minderer, M., Chettih, S. N. & Harvey, C. D. Dynamic Reorganization of Neuronal Activity Patterns in Parietal Cortex. *Cell* **170**, 986–999 (2017).
- Duemani Reddy, G., Kelleher, K., Fink, R. & Saggau, P. Three-dimensional random access multiphoton microscopy for functional imaging of neuronal activity. *Nature Neuroscience* **11**, 713–720 (2008).
- El-Boustani, S. & Sur, M. Response-dependent dynamics of cell-specific inhibition in cortical networks in vivo. *Nature Communications* **5**, 1–14 (2014).
- Feldmeyer, D., Lübke, J., Silver, R. A. & Sakmann, B. Synaptic connections between layer 4 spiny neurone-layer 2/3 pyramidal cell pairs in juvenile rat barrel cortex: Physiology and anatomy of interlaminar signalling within a cortical column. *Journal of Physiology* **538**, 803–822 (2002).
- Felleman, D. J. & Van Essen, D. C. Distributed hierarchical processing in the primate cerebral cortex. *Cerebral Cortex* **1**, 1–47 (1991).
- Friedrich, J., Zhou, P. & Paninski, L. Fast online deconvolution of calcium imaging data. *PLOS Computational Biology* **13**, e1005423 (2017).
- Fu, Y. *et al.* A cortical circuit for gain control by behavioral state. *Cell* **156**, 1139–1152 (2014).
- Gilbert, C. D. Laminar differences in receptive field properties of cells in cat primary visual cortex. *The Journal of Physiology* **268**, 391–421 (1977).
- Gilbert, C. D. Microcircuitry of the Visual Cortex. *Annual Review of Neuroscience* **6**, 217–247 (1983).
- Gill, J. V. *et al.* Precise Holographic Manipulation of Olfactory Circuits Reveals Coding Features Determining Perceptual Detection. *Neuron* **108**, 382–393 (2020).

- Gouwens, N. W. *et al.* Classification of electrophysiological and morphological neuron types in the mouse visual cortex. *Nature Neuroscience* **22**, 1182–1195 (2019).
- Grewe, B. F., Langer, D., Kasper, H., Kampa, B. M. & Helmchen, F. High-speed in vivo calcium imaging reveals neuronal network activity with near-millisecond precision. *Nature Methods* **7**, 399–405 (2010).
- Guzman, S. J., Schlögl, A., Frotscher, M. & Jonas, P. Synaptic mechanisms of pattern completion in the hippocampal CA3 network. *Science* **353**, 1117–1123 (2016).
- Harris, K. D. & Mrsic-Flogel, T. D. Cortical connectivity and sensory coding. *Nature* **503**, 51–58 (2013).
- Harris, K. D. & Shepherd, G. M. The neocortical circuit: Themes and variations. *Nature Neuroscience* **18**, 170–181 (2015).
- Harris, J. A. *et al.* Hierarchical organization of cortical and thalamic connectivity. *Nature* **575** (2019).
- Harvey, C. D., Coen, P. & Tank, D. W. Choice-specific sequences in parietal cortex during a virtual-navigation decision task. *Nature* **484**, 62–68 (2012).
- Hernandez, O. *et al.* Three-dimensional spatiotemporal focusing of holographic patterns. *Nature Communications* **7**, 1–10 (2016).
- Hofer, S. B. *et al.* Differential connectivity and response dynamics of excitatory and inhibitory neurons in visual cortex. *Nature Neuroscience* **14**, 1045–1052 (2011).
- Hubel, D. N. & Wiesel, T. N. Receptive fields, binocular interaction and functional architecture in the cat's visual cortex. *Journal of Physiology* **160**, 106–154 (1962).
- Jones, J. P. & Palmer, L. A. The two-dimensional spatial structure of simple receptive fields in cat striate cortex. *Journal of Neurophysiology* **58**, 1187–1211 (1987).
- Kafashan, M. M. *et al.* Scaling of sensory information in large neural populations shows signatures of information-limiting correlations. *Nature Communications* **12**, 1–16 (2021).
- Kalatsky, V. A. & Stryker, M. P. New paradigm for optical imaging: Temporally encoded maps of intrinsic signal. *Neuron* **38**, 529–545 (2003).
- Katona, G. *et al.* Fast two-photon in vivo imaging with three-dimensional random-access scanning in large tissue volumes. *Nature Methods* **9**, 201–208 (2012).
- Keller, D., Erö, C. & Markram, H. Cell Densities in the Mouse Brain: A Systematic Review. *Frontiers in Neuroanatomy* **12** (2018).
- Keller, G. B., Bonhoeffer, T. & Hübener, M. Sensorimotor Mismatch Signals in Primary Visual Cortex of the Behaving Mouse. *Neuron* **74**, 809–815 (2012).

- Kerlin, A. M., Andermann, M. L., Berezovskii, V. K. & Reid, R. C. Broadly Tuned Response Properties of Diverse Inhibitory Neuron Subtypes in Mouse Visual Cortex. *Neuron* **67**, 858–871 (2010).
- Khan, A. G. & Hofer, S. B. Contextual signals in visual cortex. *Current Opinion in Neurobiology* **52**, 131–138 (2018).
- Ko, H. *et al.* Functional specificity of local synaptic connections in neocortical networks. *Nature* **473**, 87–91 (2011).
- Kohn, A. & Smith, M. A. Stimulus dependence of neuronal correlation in primary visual cortex of the macaque. *Journal of Neuroscience* **25**, 3661–3673 (2005).
- Kondo, S. & Ohki, K. Laminar differences in the orientation selectivity of geniculate afferents in mouse primary visual cortex. *Nature Neuroscience* **19**, 316–319 (2016).
- Kvitsiani, D. *et al.* Distinct behavioural and network correlates of two interneuron types in prefrontal cortex. *Nature* **498**, 363–366 (2013).
- Lee, K. S., Huang, X. & Fitzpatrick, D. Topology of on and off inputs in visual cortex enables an invariant columnar architecture. *Nature* **533**, 90–94 (2016).
- Lefort, S., Tomm, C., Floyd Sarria, J.-C. & Petersen, C. C. The Excitatory Neuronal Network of the C2 Barrel Column in Mouse Primary Somatosensory Cortex. *Neuron* **61**, 301–316 (2009).
- Li, L. Y., Li, Y. T., Zhou, M., Tao, H. W. & Zhang, L. I. Intracortical multiplication of thalamocortical signals in mouse auditory cortex. *Nature Neuroscience* **16**, 1179–1181 (2013).
- Li, Y.-t. *et al.* Broadening of Inhibitory Tuning Underlies Contrast-Dependent Sharpening of Orientation Selectivity in Mouse Visual Cortex. *Journal of Neuroscience* **32**, 16466–16477 (2012).
- Li, Y.-t., Liu, B.-h., Chou, X.-l., Zhang, L. I. & Tao, H. W. Synaptic Basis for Differential Orientation Selectivity between Complex and Simple Cells in Mouse Visual Cortex. *Journal of Neuroscience* **35**, 11081–11093 (2015).
- Li, Y. T., Ibrahim, L. A., Liu, B. H., Zhang, L. I. & Tao, H. W. Linear transformation of thalamocortical input by intracortical excitation. *Nature Neuroscience* **16**, 1324–1330 (2013).
- Lien, A. D. & Scanziani, M. Tuned thalamic excitation is amplified by visual cortical circuits. *Nature Neuroscience* **16**, 1315–1323 (2013).
- Lim, S. T., Antonucci, D. E., Scannevin, R. H. & Trimmer, J. S. A novel targeting signal for proximal clustering of the Kv2.1 K<sup>+</sup>channel in hippocampal neurons. *Neuron* **25**, 385–397 (2000).
- Lu, R. *et al.* Video-rate volumetric functional imaging of the brain at synaptic resolution. *Nature Neuroscience* **20**, 620–628 (2017).

- Ma, W.-p. *et al.* Visual Representations by Cortical Somatostatin Inhibitory Neurons—Selective But with Weak and Delayed Responses. *Journal of Neuroscience* **30**, 14371–14379 (2010).
- Madisen, L. *et al.* A robust and high-throughput Cre reporting and characterization system for the whole mouse brain. *Nature Neuroscience* **13**, 133–140 (2010).
- Makino, H. & Komiyama, T. Learning enhances the relative impact of top-down processing in the visual cortex. *Nature Neuroscience* **18**, 1116–1122 (2015).
- Malina, K. C. K., Mohar, B., Rappaport, A. N. & Lampl, I. Local and thalamic origins of correlated ongoing and sensory-evoked cortical activities. *Nature Communications* **7**, 1–11 (2016).
- Mardinly, A. R. *et al.* Precise multimodal optical control of neural ensemble activity. *Nature Neuroscience* **21**, 881–893 (2018).
- Markram, H., Lubke, J., Frotscher, M. & Sakmann, B. Regulation of Synaptic Efficacy by Coincidence of Postsynaptic APs and EPSPs. *Science* **275**, 213–215 (1997).
- Marshel, J. H., Kaye, A. P., Nauhaus, I. & Callaway, E. M. Anterior-Posterior Direction Opponency in the Superficial Mouse Lateral Geniculate Nucleus. *Neuron* **76**, 713–720 (2012).
- Marshel, J. H. *et al.* Cortical layer-specific critical dynamics triggering perception. *Science* **5202**, eaaw5202 (2019).
- Martinez, L. M. & Alonso, J. M. Construction of complex receptive fields in cat primary visual cortex. *Neuron* **32**, 515–525 (2001).
- Martinez, L. M. *et al.* Receptive field structure varies with layer in the primary visual cortex. *Nature Neuroscience* **8**, 372–379 (2005).
- Miller, K. D. Canonical computations of cerebral cortex. *Current Opinion in Neurobiology* **37**, 75–84 (2016).
- Minderer, M., Brown, K. D. & Harvey, C. D. The Spatial Structure of Neural Encoding in Mouse Posterior Cortex during Navigation. *Neuron* **102**, 232–248 (2019).
- Mooser, F., Bosking, W. H. & Fitzpatrick, D. A morphological basis for orientation tuning in primary visual cortex. *Nature Neuroscience* **7**, 872–879 (2004).
- Morgenstern, N. A., Bourg, J. & Petreanu, L. Multilaminar networks of cortical neurons integrate common inputs from sensory thalamus. *Nature Neuroscience* **19**, 1034–1040 (2016).
- Niell, C. M. & Stryker, M. P. Highly Selective Receptive Fields in Mouse Visual Cortex. *Journal of Neuroscience* **28**, 7520–7536 (2008).
- Niell, C. M. & Stryker, M. P. Modulation of Visual Responses by Behavioral State in Mouse Visual Cortex. *Neuron* **65**, 472–479 (2010).
- Ohki, K., Chung, S., Ch'ng, Y. H., Kara, P. & Reid, R. C. Functional imaging with cellular resolution reveals precise microarchitecture in visual cortex. *Nature* **433**, 597–603 (2005).



- Okun, M. *et al.* Diverse coupling of neurons to populations in sensory cortex. *Nature* **521**, 511–515 (2015).
- Olshausen, B. A. & Fieldt, D. J. Sparse Coding with an Overcomplete Basis Set: A Strategy Employed by V1? *Vision Res* **37**, 3311–3325 (1997).
- Olshausen, B. A. & Field, D. J. Sparse coding of sensory inputs. *Current Opinion in Neurobiology* **14**, 481–487 (2004).
- Oron, D., Tal, E. & Silberberg, Y. Scanningless depth-resolved microscopy. *Optics Express* **13**, 1468–1476 (2005).
- Packer, A. M. & Yuste, R. Dense, Unspecific Connectivity of Neocortical Parvalbumin-Positive Interneurons: A Canonical Microcircuit for Inhibition? *Journal of Neuroscience* **31**, 13260–13271 (2011).
- Packer, A. M. *et al.* Two-photon optogenetics of dendritic spines and neural circuits. *Nature Methods* **9**, 1202–1205 (2012).
- Packer, A. M., Russell, L. E., Dalglish, H. W. & Häusser, M. Simultaneous all-optical manipulation and recording of neural circuit activity with cellular resolution in vivo. *Nature Methods* **12**, 140–146 (2015).
- Pakan, J. M. *et al.* Behavioral-state modulation of inhibition is context-dependent and cell type specific in mouse visual cortex. *eLife* **5**, 1–18 (2016).
- Papagiakoumou, E. *et al.* Scanless two-photon excitation of channelrhodopsin-2. *Nature Methods* **7**, 848–854 (2010).
- Papagiakoumou, E., Ronzitti, E. & Emiliani, V. Scanless two-photon excitation with temporal focusing. *Nature Methods* **17**, 571–581 (2020).
- Pégar, N. C. *et al.* Three-dimensional scanless holographic optogenetics with temporal focusing (3D-SHOT). *Nature Communications* **8**, 1–14 (2017).
- Peirce, J. W. PsychoPy-Psychophysics software in Python. *Journal of Neuroscience Methods* **162**, 8–13 (2007).
- Peng, Y. *et al.* High-throughput microcircuit analysis of individual human brains through next-generation multineuron patch-clamp. *eLife* **8**, 1–52 (2019).
- Perin, R., Berger, T. K. & Markram, H. A synaptic organizing principle for cortical neuronal groups. *Proceedings of the National Academy of Sciences* **108**, 5419–5424 (2011).
- Petersen, C. C. The functional organization of the barrel cortex. *Neuron* **56**, 339–355 (2007).
- Pfeffer, C. K., Xue, M., He, M., Huang, Z. J. & Scanziani, M. Inhibition of inhibition in visual cortex: The logic of connections between molecularly distinct interneurons. *Nature Neuroscience* **16**, 1068–1076 (2013).

- Pi, H. J. *et al.* Cortical interneurons that specialize in disinhibitory control. *Nature* **503**, 521–524 (2013).
- Piscopo, D. M., El-Danaf, R. N., Huberman, A. D. & Niell, C. M. Diverse Visual Features Encoded in Mouse Lateral Geniculate Nucleus. *J. Neurosci* **33**, 4642–4656 (2013).
- Podgorski, K. & Ranganathan, G. Brain heating induced by near-infrared lasers during multi-photon microscopy. *Journal of Neurophysiology* **116**, 1012–1023 (2016).
- Polack, P. O., Friedman, J. & Golshani, P. Cellular mechanisms of brain state-dependent gain modulation in visual cortex. *Nature Neuroscience* **16**, 1331–1339 (2013).
- Polat, U., Mizobe, K., Pettet, M. W., Kasamatsu, T. & Norcia, A. M. Collinear stimuli regulate visual responses depending on cell's contrast threshold. *Nature* **391**, 580–584 (1998).
- Poort, J. *et al.* Learning Enhances Sensory and Multiple Non-sensory Representations in Primary Visual Cortex. *Neuron* **86**, 1478–1490 (2015).
- Prakash, R. *et al.* Two-photon optogenetic toolbox for fast inhibition, excitation and bistable modulation. *Nature Methods* **9**, 1171–1179 (2012).
- Prevedel, R. *et al.* Fast volumetric calcium imaging across multiple cortical layers using sculpted light. *Nature Methods* **13**, 1021–1028 (2016).
- Rasmussen, C. E. & Williams, C. *Gaussian Processes for Machine Learning* (MIT Press, Cambridge, MA, 2006).
- Reinhold, K., Lien, A. D. & Scanziani, M. Distinct recurrent versus afferent dynamics in cortical visual processing. *Nature Neuroscience* **18**, 1789–1797 (2015).
- Rickgauer, J. P. & Tank, D. W. Two-photon excitation of channelrhodopsin-2 at saturation. *Proceedings of the National Academy of Sciences* **106**, 15025–15030 (2009).
- Ringach, D. L., Shapley, R. M. & Hawken, M. J. Orientation selectivity in macaque V1: Diversity and laminar dependence. *Journal of Neuroscience* **22**, 5639–5651 (2002).
- Robinson, N. T. *et al.* Targeted Activation of Hippocampal Place Cells Drives Memory-Guided Spatial Behavior. *Cell* **183**, 1586–1599 (2020).
- Rosenbaum, R., Smith, M. A., Kohn, A., Rubin, J. E. & Doiron, B. The spatial structure of correlated neuronal variability. *Nature Neuroscience* **20**, 107–114 (2017).
- Rossi, L. F., Harris, K. D. & Carandini, M. Spatial connectivity matches direction selectivity in visual cortex. *Nature* **2019** (2020).
- Runyan, C. A. *et al.* Response Features of Parvalbumin-Expressing Interneurons Suggest Precise Roles for Subtypes of Inhibition in Visual Cortex. *Neuron* **67**, 847–857 (2010).
- Saleem, A. B., Ayaz, A., Jeffery, K. J., Harris, K. D. & Carandini, M. Integration of visual motion and locomotion in mouse visual cortex. *Nature Neuroscience* **16**, 1864–1869 (2013).

- Scala, F. *et al.* Layer 4 of mouse neocortex differs in cell types and circuit organization between sensory areas. *Nature Communications* **10**, 4174 (2019).
- Scholl, B., Tan, A. Y. Y., Corey, J. & Priebe, N. J. Emergence of Orientation Selectivity in the Mammalian Visual Pathway. *Journal of Neuroscience* **33**, 10616–10624 (2013).
- Seeman, S. C. *et al.* Sparse recurrent excitatory connectivity in the microcircuit of the adult mouse and human cortex. *eLife* **7**, 1–27 (2018).
- Shemesh, O. A. *et al.* Temporally precise single-cell-resolution optogenetics. *Nature Neuroscience* **20**, 1796–1806 (2017).
- Shepherd, G. M. G. Laminar and Columnar Organization of Ascending Excitatory Projections to Layer 2/3 Pyramidal Neurons in Rat Barrel Cortex. *Journal of Neuroscience* **25**, 5670–5679 (2005).
- Smith, S. L. & Häusser, M. Parallel processing of visual space by neighboring neurons in mouse visual cortex. *Nature Neuroscience* **13**, 1144–1149 (2010).
- Somers, D., Nelson, S. & Sur, M. An emergent model of orientation selectivity in cat visual cortical simple cells. *The Journal of Neuroscience* **15**, 5448–5465 (1995).
- Song, A. *et al.* Volumetric two-photon imaging of neurons using stereoscopy (vtwins). *Nature Methods* **14**, 420–426 (2017).
- Song, S., Sjöström, P. J., Reigl, M., Nelson, S. & Chklovskii, D. B. Highly Nonrandom Features of Synaptic Connectivity in Local Cortical Circuits. *PLoS Biology* **3**, e68 (2005).
- Steinmetz, N. A. *et al.* Aberrant Cortical Activity In Multiple GCaMP6-Expressing Transgenic Mouse Lines. *eNeuro* **4**, 1–15 (2017).
- Sun, W., Tan, Z., Mensh, B. D. & Ji, N. Thalamus provides layer 4 of primary visual cortex with orientation- and direction-tuned inputs. *Nature Neuroscience* **19**, 308–315 (2016).
- Tasic, B. *et al.* Adult mouse cortical cell taxonomy revealed by single cell transcriptomics. *Nature Neuroscience* **19**, 335–346 (2016).
- Tasic, B. *et al.* Shared and distinct transcriptomic cell types across neocortical areas. *Nature* **563**, 72–78 (2018).
- Thomson, A. M. Functional maps of neocortical local circuitry. *Frontiers in Neuroscience* **1**, 19–42 (2007).
- Vladimirov, N. *et al.* Brain-wide circuit interrogation at the cellular level guided by online analysis of neuronal function. *Nature Methods* **15**, 1117–1125 (2018).
- Van Vreeswijk, C. & Sompolinsky, H. Chaos in neuronal networks with balanced excitatory and inhibitory activity. *Science* **274**, 1724–1726 (1996).

- de Vries, S. E. J. *et al.* A large-scale standardized physiological survey reveals functional organization of the mouse visual cortex. *Nature Neuroscience* **23**, 138–151 (2020).
- Wekselblatt, J. B., Flister, E. D., Piscopo, D. M. & Niell, C. M. Large-scale imaging of cortical dynamics during sensory perception and behavior. *Journal of Neurophysiology* **115**, 2852–2866 (2016).
- Wertz, A. *et al.* layer-specific cortical Network Modules. *Science* **349**, 70–74 (2015).
- Wilson, N. R., Runyan, C. A., Wang, F. L. & Sur, M. Division and subtraction by distinct cortical inhibitory networks in vivo. *Nature* **488**, 343–348 (2012).
- Xu, H., Jeong, H. Y., Tremblay, R. & Rudy, B. Neocortical Somatostatin-Expressing GABAergic Interneurons Disinhibit the Thalamorecipient Layer 4. *Neuron* **77**, 155–167 (2013).
- Yang, G. R., Murray, J. D. & Wang, X. J. A dendritic disinhibitory circuit mechanism for pathway-specific gating. *Nature Communications* **7** (2016).
- Yang, W., Carrillo-Reid, L., Bando, Y., Peterka, D. S. & Yuste, R. Simultaneous two-photon imaging and two-photon optogenetics of cortical circuits in three dimensions. *eLife* **7**, 1–21 (2018).
- Yatsenko, D., Walker, E. Y. & Tolia, A. S. DataJoint: A Simpler Relational Data Model. *arXiv* (2018).
- Yoshida, T. & Ohki, K. Natural images are reliably represented by sparse and variable populations of neurons in visual cortex. *Nature Communications* **11** (2020).
- Yoshimura, Y., Dantzker, J. L. M. & Callaway, E. M. Excitatory cortical neurons form fine-scale functional networks. *Nature* **433**, 868–873 (2005).
- Yoshimura, Y. & Callaway, E. M. Fine-scale specificity of cortical networks depends on inhibitory cell type and connectivity. *Nature Neuroscience* **8**, 1552–1559 (2005).
- Yu, B. M. *et al.* Gaussian-process factor analysis for low-dimensional single-trial analysis of neural population activity. *Journal of Neurophysiology* **102**, 614–635 (2009).
- Zhao, X., Chen, H., Liu, X. & Cang, J. Orientation-selective Responses in the Mouse Lateral Geniculate Nucleus. *Journal of Neuroscience* **33**, 12751–12763 (2013).
- Zhu, G., Howe, J., Durst, M., Zipfel, W. & Xu, C. Simultaneous spatial and temporal focusing of femtosecond pulses. *Optics InfoBase Conference Papers* **13**, 2153–2159 (2005).
- Znamenskiy, P. *et al.* Functional selectivity and specific connectivity of inhibitory neurons in primary visual cortex. *bioRxiv* (2018).